From half-cells to full-cells: across-scale comparative evaluation of lanthanum-based perovskites as high-performance anode materials for the oxygen evolution reaction

Blaž Toplak[a,§], Leon Müller[b,§], Ali Raza Khan[c], André Olean-Oliveira[c], Khuzaifa Yahuza Muhammad[d], Wang Feng[e], Raíssa Ribeiro Lima Machado[f], Da Xing[e], Mohammed-Ali Sheikh[b], Leander Kucklick[e], Ahammed Suhail Odungat[a], Adarsh Jain[a], Lars Grebener[a], Philipp Gerschel[d], Corina Andronescu[f,g], Harry Hoster[e,g,h], Christof Schulz[b,g], Viktor Čolić[c,g], Ulf-Peter Apfel[d,i], Hartmut Wiggers[b,g], Mohaned Hammad[a*], and Doris Segets[a,g,*]

[a] *Institute for Energy and Materials Processes – Particle Science and Technology, University of Duisburg-Essen, 47057 Duisburg, Germany*
[b] *Institute for Energy and Materials Processes – Reactive Fluids, University of Duisburg-Essen, 47057 Duisburg, Germany*
[c] *Electrochemistry for Energy Conversion, Max Planck Institute for Chemical Energy Conversion, 45470 Mülheim an der Ruhr, Germany*
[d] *Activation of Small Molecules – Technical Electrochemistry, Ruhr-Universität Bochum, 44801 Bochum, Germany*
[e] *Energy Technology, University of Duisburg-Essen, 47057 Duisburg, Germany*
[f] *Chemical Technology III, Faculty of Chemistry, University of Duisburg-Essen, 47057 Duisburg, Germany*
[g] *Center for Nanointegration Duisburg-Essen, University of Duisburg-Essen, 47057 Duisburg, Germany*
[h] *The Hydrogen and Fuel Cell Center ZBT GmbH, 47057 Duisburg, Germany*
[i] *Department of Electrosynthesis, Fraunhofer UMSICHT, 46047 Oberhausen, Germany*

[*]Corresponding authors.
E-mail addresses: doris.segets@uni-due.de (D. Segets), mohaned.hammad@uni-due.de (M. Hammad)

[§] These authors contributed equally to this paper.

ABSTRACT

The widespread reliance on evaluating electrocatalysts in electrochemical half-cells presents limitations that hinder a faster transition from academia to industry and can lead to premature exclusion of promising materials. To address these challenges, it is crucial to implement materials testing in application-relevant setups such as zero-gap full-cells. This transition can be achieved through implementing coherent workflows combining rapid evaluation of as-synthesized materials, electrode evaluation at different scales, and post-mortem analysis. This work presents a comparative study of three spray-flame synthesized lanthanum-based perovskite materials ($LaMnO_3$, $LaFeO_3$, and $LaCoO_3$) for the oxygen evolution reaction under alkaline conditions, highlighting different behavior across scales. The research demonstrates how the interplay of materials properties, electrode engineering, and metal–support interactions influences performance under mild and harsh electrochemical conditions. Electrochemical half-cell testing consistently identifies $LaFeO_3$ as the best oxygen evolution reaction catalyst across various configurations. This unforeseen behavior necessitates further investigation under application-relevant conditions. Full-cell testing at 500 mA cm^{-2} corroborates the trends observed in electrochemical half-cell testing, with $LaFeO_3$ and $LaMnO_3$ exhibiting comparable performance to $LaCoO_3$ after prolonged operation. Furthermore, a degradation study under 1000 mA cm^{-2} highlights their potential for continued catalyst development. Advanced post-mortem techniques provide deeper insight into catalytic activity and structural changes, linking performance evolution to catalyst–substrate interactions and material-dependent surface changes under oxidative polarization. By bridging fundamental studies to application-relevant testing, this research provides knowledge and methods for accelerated material and electrode development.

Keywords: zero-gap full-cell, coherent workflow, spray-flame synthesis, perovskite material, oxygen evolution reaction, alkaline water electrolysis

1. Introduction

Water electrolysis consists of water decomposition into hydrogen and oxygen through an external energy-driven redox reaction. The oxygen evolution reaction (OER) at the anode is kinetically sluggish and represents a major bottleneck in the development of highly efficient anode electrocatalysts. Noble metals, such as Ir and Ru, exhibit adequate OER performance in acidic conditions. However, their scarcity, high cost, and limited stability hinder their practical applications [1–4]. In contrast, electrolysis in alkaline conditions can be performed with various non-noble metal materials with decent stability. Among them, mixed spinel oxides and metal organic frameworks (MOF)-derived composites have attracted attention due to their tunable composition and structural versatility [5–7]. Along this line, perovskite oxide materials (ABO_3, where A represents alkaline-earth or rare-earth metals {Ca, Sr, La} and B represents transition metals {Mn, Fe, Co, and Ni}) have shown promising results in alkaline OER [4,8–11]. For instance, La-based perovskites possess the advantage of structural flexibility in the A and B positions, which affects conductivity, stability, and defect formation [12,13].

In this study, we focus on three La-based perovskites: $LaMnO_3$, $LaFeO_3$, and $LaCoO_3$ (LMO, LFO, and LCO). The increase of the $Mn^{4+/3+}$ ratio in LMO induces more oxygen bonding with the active Mn^{4+}, leading to improved structural stabilization [14,15]. LFO combines good redox activity with suitable electronic and ionic conductivity [16]. However, LCO offers superior intrinsic catalytic activity compared to the other two candidates due to the $Co^{3+/4+}$ redox transitions, which promote the formation of oxygen vacancies in the lattice [12,17]. Although several OER studies have investigated previously mentioned perovskites [18–21], they have typically only been evaluated at laboratory-scale conditions using rotating disc electrodes (RDE) or on nickel foam at low current densities of 10 mA cm^{-2}, with LCO consistently presented as the best pristine perovskite for OER [18–20,22]. As a result, the systematic transferability of these activity trends to application-relevant conditions remains largely

unexplored. In these studies, the perovskite materials were prepared via solution combustion, sol-gel, or co-precipitation synthesis.

In contrast, this work introduces spray-flame synthesized perovskites. Spray-flame synthesis (SFS) has proven to be a highly effective and innovative approach for producing nanosized lanthanum-based perovskites [23], offering distinct advantages over traditional methods such as solid-state synthesis, solution combustion, and sol-gel synthesis [24,25]. In terms of preparation cost, SFS generally enables faster processes with reduced energy consumption [26], thus lowering operational expenses compared to sol-gel and solution combustion, which often require longer reaction times and higher post-processing temperatures. Solid-state synthesis is not the preferred method because nanoparticles with a high specific surface, which is aimed for in applications such as catalysis, cannot be obtained. The scalability of SFS is superior, as it can be continuously operated and readily transferred to large-scale production [27,28], whereas sol-gel and solution combustion methods are often batch-based and more challenging to scale up [29]. Although batches can be scaled up in sol-gel synthesis, maintaining high phase purity and small particle sizes remains a significant challenge [30]. Furthermore, the use of liquid precursors in SFS enables efficient molecular-level mixing of metal ions, thereby facilitating precise control over the particles' composition. Importantly, the use of SFS allows us to minimize morphological and structural variability between LMO, LFO, and LCO, thereby decoupling intrinsic material chemistry from extrinsic synthesis-induced effects.

Advancing technology for alkaline water splitting, and in particular for the OER, requires more than just understanding the intrinsic properties of the synthesized materials. It also involves addressing the associated challenges connected to anode preparation, which arise in the case of particle-based, coated catalyst layers due to complex interactions among the substrate, ionomer, and electrocatalyst. Factors such as ink formulation, ink deposition, substrate selection, and electrocatalyst properties influence adhesion, cohesion, wetting, and overall efficiency [31,32]. This creates a highly complicated system that requires a tailored approach for each

electrocatalyst [33]. Another barrier is the slow transition from lab-scale testing in electrochemical half-cells (10-100 mA cm^{-2}, room temperature) toward industry-relevant testing using full-cells ($\geq$ 500 mA cm^{-2}, $\geq$ 50 °C) [34]. This hinders the integration of electrocatalysts into real-life systems early in the product and process development due to a limited understanding of the material's behavior. To overcome these challenges, we previously developed a highly structured and coherent workflow that enables the evaluation of electrocatalyst performance (half- and full-cell testing) in combination with a systematic and trackable material assessment along the process chain, using scalable technologies [33]. This comprehensive approach integrates synthesis, advanced ink formulation, electrochemical testing, and electrode post-mortem analysis, pointing towards pathways for future materials development. In addition to meeting material preparation requirements on a desired scale and with the desired activity and stability, practical OER catalysts must also meet industrial criteria, including cost-effectiveness, appropriate selection of membranes, the use of earth-abundant and low-toxic elements, minimal environmental impact, and compliance with government policies. While these factors are crucial for large-scale water electrolysis, they are beyond the scope of the current study and do not represent a comprehensive list of all considerations necessary for real-world implementation [35–37].

In this research, we emphasize that advancing perovskite-based OER anodes requires bridging the gap between laboratory-scale screening and application-relevant operation. While intrinsic electronic structure and redox properties provide an important baseline, the apparent activity and stability of particle-based perovskite electrodes can be strongly influenced by electrode preparation and by material evolution under oxidative polarization. Therefore, we combine spray-flame synthesis with controlled electrode fabrication and a coherent evaluation workflow spanning complementary half-cell configurations and zero-gap full-cell testing, supported by post-mortem characterization. This integrated approach enables a systematic comparison of LMO, LFO, and LCO and establishes a mechanistic framework for understanding how

perovskite composition, catalyst–substrate interactions, and surface evolution shape OER performance across operating regimes.

2. Experimental Section

2.1. Spray-flame synthesized perovskites

LMO, LFO, and LCO nanoparticles were synthesized via spray-flame synthesis using a SpraySyn-based reactor, following procedures established in our previous studies [33,38]. The precursors, solvents, and binder were obtained from commercial suppliers. A complete list of chemicals and sources, as well as details of precursor preparation and reactor conditions, is provided in Section S1.1 (supplementary material).

2.2. Construction of catalyst-coated electrodes

Catalyst-coated anode electrodes were prepared by ultrasonic spray coating perovskite-based inks onto nickel substrates (plate and foam). The final catalyst loading for all electrochemical experiments was 0.25-0.26 μg cm^{-2}. Due to system requirements, the mass loading for the flow cell coupled with inductively coupled plasma optical emission spectroscopy (ICP-OES) was 1 mg cm^{-2}. The anode electrode fabrication process is described in detail in Section S1.2 (supplementary material).

2.3. Characterization of perovskite nanopowders and anode electrodes

Structural characteristics of the synthesized nanoparticles were characterized using X-ray diffraction (XRD), Raman spectroscopy, transmission electron microscopy (TEM), and a high-resolution TEM (HRTEM), equipped with energy-dispersive X-ray analysis (EDX) for elemental mapping. X-ray photoelectron spectroscopy (XPS) was used for the evaluation of the surface elemental composition. The specific surface area and porosity of LSCO materials were

evaluated by N_2 physisorption measurements using the Brunauer-Emmett-Teller (BET) method, while surface functional groups were probed by attenuated total reflectance Fourier transform infrared spectroscopy (ATR-FTIR). The stability of the nanoparticle dispersions over time was evaluated using an analytical centrifuge (LUMiSizer®). Additionally, perovskite-based electrodes were assessed using a scanning electron microscope (SEM). The morphology of the fabricated coatings was inspected using an atomic force microscope (AFM), while XRD patterns were recorded in grazing incidence mode (GIXRD). Surface wettability was assessed using contact angle measurements, and coating adhesion strength was evaluated using centrifugal detachment. Comprehensive characterization methods are described in Section S1.3 (supporting Information).

2.4. Electrochemical measurements

The electrocatalytic OER performance in various electrochemical half-cells was evaluated in O_2-saturated, 1 M KOH. All measured potentials were automatically 85 % iR_u-corrected and referenced to the reversible hydrogen electrode (RHE) [33]. Electrochemical tests included electrochemical impedance spectroscopy (EIS), cyclic voltammetry (CV), linear sweep voltammetry (LSV), and chronopotentiometry (CP). The membrane electrode assembly (MEA) used in the full-cell measurements consisted of catalyst-coated nickel foams on the anodic side and Pt-coated carbon paper on the cathodic side, with PiperION-HCO3 serving as the membrane. The detailed experimental procedures are provided in Section S1.4 (supporting information).

3. Results and discussion

3.1. Catalytic nanopowder characterization

All three perovskite materials were synthesized using SFS with identical solvents and concentration ratios of the respective precursors. Their structures and compositions were analyzed using XRD (Figure 1a) and Raman spectroscopy (Figure 1b). LMO and LFO diffraction peaks can be indexed to the single-phase orthorhombic structure matching ICSD 51653 and ICSD 7794, respectively [39–42]. Conversely, the diffraction pattern of LCO matches the rhombohedral perovskite $LaCoO_{2.925}$ structure (ICSD 153993) [21]. The phase compositions of the perovskite materials were additionally assessed with Raman spectroscopy at room temperature, which has the advantage of being more sensitive to oxygen motion and structure distortion [43,44]. The Raman spectra of LMO reveal two strong vibrational modes at around 495 and 622 cm^{-1}, which are attributed to the Jahn-Teller distortion of MnO_6 octahedra [45,46]. Likewise, in the LFO, Raman modes at 435 cm^{-1} are related to oxygen bending vibrations, while stretching Raman modes of FeO_6 octahedra are observed at 636 cm^{-1}. These findings for both materials are consistent with the orthorhombic structural configuration previously determined through XRD [47–49]. Furthermore, the Raman mode in LCO at 640 cm^{-1} corresponds to Co–O stretching vibrations, providing additional support for the rhombohedral arrangement of LCO [50,51].

To investigate the surface properties and valence states of all three perovskite powders, XPS analysis was performed. In all cases, lanthanum (supplementary material, Figure S1a) is present as La^{3+}. The La $3d_{5/2}$ multiplet splitting shows energy differences of 3.7, 3.7, and 3.8 eV for LMO, LFO, and LCO, respectively. These values are consistent with those reported in the literature for lanthanum-based perovskites [52–54]. The surface spectra of Mn $2p_{3/2}$ (supplementary material, Figure S1b) deconvoluted by peaks at 641.1 and 642.8 eV, belong to Mn^{3+} and Mn^{4+} species, where manganese is predominantly in the Mn^{3+} valence state [55,56]. The two Fe $2p_{3/2}$ peaks (supplementary material, Figure S1c) positioned at around 710.2 and

711.9 eV indicate the presence of a mixed oxidation state of Fe^{2+} and Fe^{3+}, respectively [57]. The Co $2p_{3/2}$ (supplementary material, Figure S1d) spectra are also fitted with two individual peaks at 779.7 and 781.4 eV, corresponding to the Co^{3+} and Co^{2+} oxidation states [38,58]. The main O 1s XPS spectra for all materials were deconvoluted into two components (supplementary material, Figure S1e) at approximately 528.8 and 531.5 eV, respectively, indicating predominantly lattice oxygen ($O_{lattice}$) and adsorbed hydroxyl species ($O_{surface}$) on the surface [38,59,60].

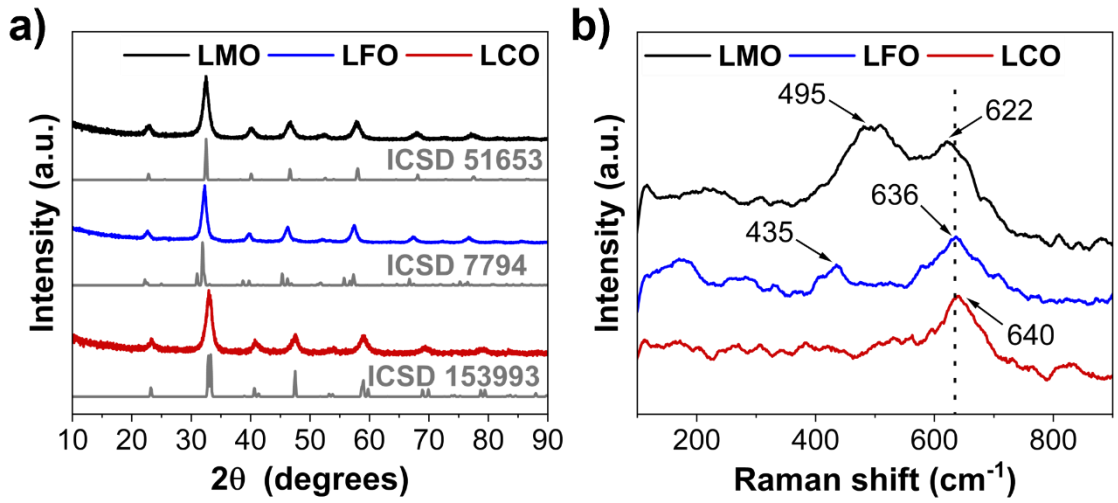

Figure 1. (a) XRD patterns of spray-flame synthesized LMO (black), LFO (blue), and LCO (red), with corresponding ICSD references 51653, 7794, and 153993 (grey). (b) Raman spectra of LMO (black), LFO (blue), and LCO (red).

The morphological and elemental analysis of spray-flame synthesized perovskite materials was performed using TEM and EDX (Figure 2a–c, supplementary material, Figure S2a–c). All three materials are confirmed to be mainly present as quasi-spherical primary nanoparticles with distinct edges, while the EDX analysis evidences a uniform elemental distribution in all three perovskites. Furthermore, HRTEM images of LMO and LFO (Figure 2d–e) show interplanar spacing of 0.281 nm for LMO, corresponding to the (011) orthorhombic lattice plane, and 0.285 and 0.395 nm for LFO, matching the (121) and (101) lattice planes, respectively [61,62].

Moreover, the HRTEM image of LCO (Figure 2f) exhibits crystal lattice fringes with an interlayer spacing of 0.273 nm, corresponding to (104) rhombohedral planes, consistent with the XRD and Raman spectroscopy analysis [63,64]. Additionally, the specific surface area was examined using the BET method. Moreover, SEM analysis (supplementary material, Figure S3) reveals that all three perovskites tend to agglomerate due to van der Waals forces, particularly when analyzed as dry powders. The measured specific surface of LMO, LFO, and LCO was 105.2, 94.2, and 84.6 $m^2\ g^{-1}$, with corresponding calculated primary particle sizes (x_p^{BET}) of 8.7, 9.6, and 10.0 nm, respectively. In total, utilizing the spray flame at high temperatures results in improved intrinsic properties and phase-pure perovskite structures with a high surface area. This is crucial for enhancing the accessibility of active sites. The process temperature can be influenced by several parameters, including solvent type, fuel flow, oxygen-to-fuel ratio, and precursor concentration. Our previous studies have shown that adding methane to the dispersion gas reduces surface contamination from residual carbonaceous species. Additionally, precursor concentration has a significantly greater influence on particle size and distribution than other process parameters [65]. However, the use of high-temperature solvents such as toluene and xylol restricts precursor selection, as nitrate-based compounds are incompatible.

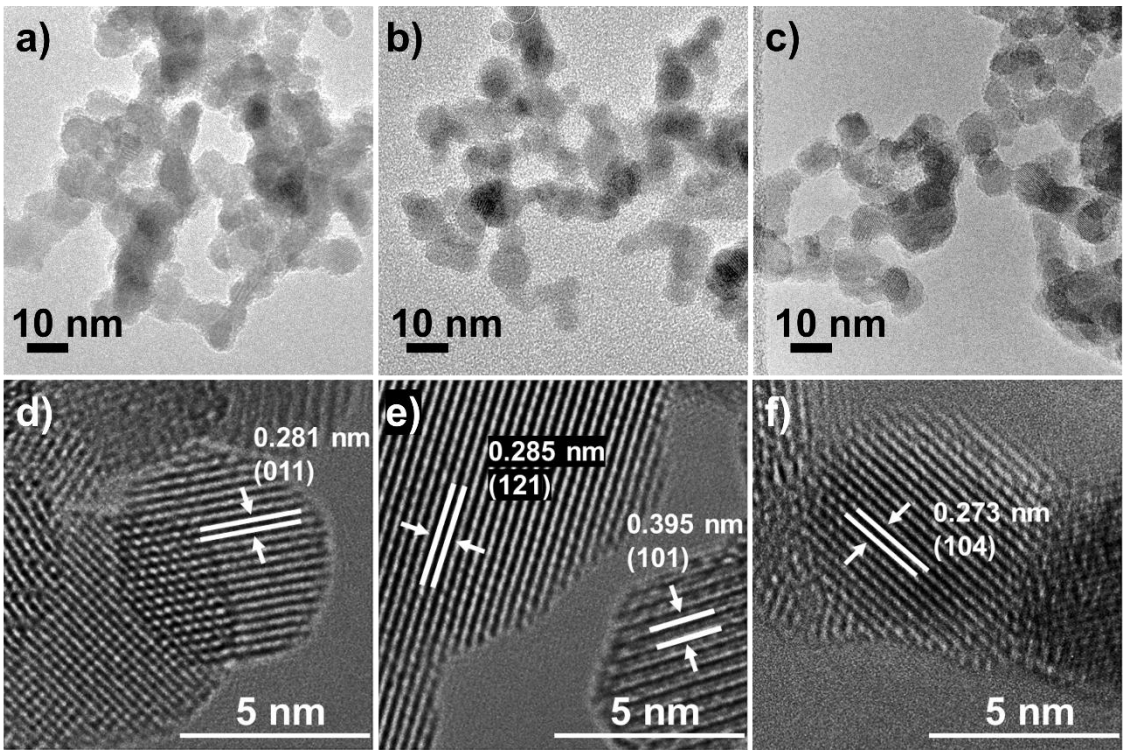

Figure 2. (a-c) TEM images of LMO, LFO, and LCO nanopowders. (d-f) HRTEM images of LMO, LFO, and LCO perovskite materials.

3.2. Powder wetting, dispersion, and ink characterization

Understanding the interactions between nanoparticles, additives, and solvents is crucial for achieving uniform electrode fabrication and a successful transition from lab-scale to larger-scale processes. Moreover, the ability to control the electrode structure for three perovskite materials is crucial for enabling direct comparison of the materials in half- and full-cells. The key to a smooth transition is the preparation of homogeneous, stable dispersions from non-toxic, environmentally and economically feasible solvents and additives/binders. To investigate the interactions of LMO, LFO, and LCO nanoparticles with different solvents or probe liquids (PLs), the method of Hanson Solubility Parameter (HSP) was employed, which we have previously adopted to assess particulates [66,67]. Thereby, the selection of PLs plays a crucial role in determining the surface properties of perovskite nanoparticles. For that reason, a two-step method developed by Amin et al. [68] was introduced. Each of the perovskite powders was

initially dispersed in polar protic, polar aprotic, and moderately polar PLs, including ethanol, dimethylformamide, tetrahydrofuran, 2-propanol, dimethyl sulfoxide, and acetone. The interactions and stability of perovskite nanoparticles in the PLs were visualized using transmittograms (supplementary material, Figure S4–S6), which provide qualitative and quantitative insights into the physical properties of complex colloidal or dispersed systems [69]. For the calculation of the HSP sphere, the interaction of perovskites with different PLs was finally categorized on the basis of relative sedimentation times of the settling dispersion during analytical centrifugation. Using the HSPiP software and the automated addition method developed by Süß et al. [70] and Anwar et al. [71], the ordering of PLs into good and poor was done (supplementary material, Figure S7).

Transmittograms reveal similar interactions in LMO and LFO, resulting in the same PL ranking and HSP. Both materials demonstrate good dispersibility in polar protic ethanol and 2-propanol, as well as polar aprotic dimethylformamide. In contrast, moderate polar PLs tetrahydrofuran, acetone, and polar aprotic dimethylsulfoxide, are classified as poor. LCO exhibits good dispersion stability in polar protic ethanol and polar aprotic dimethylformamide and dimethylsulfoxide, while 2-propanol, tetrahydrofuran, and acetone are classified as poor. Differences in HSP are explained by distinct crystal structures, which affect the interactions between the nanoparticle surface and the probe liquid molecules [66,72,73]. These differences are reflected in the elevated δ_D and δ_P values of LCO compared to LMO and LFO, resulting in a larger radius of the Hansen sphere (supplementary material, Figure S7, Table S1).

For further understanding of the interaction between perovskites and PLs, Fourier-transform infrared spectroscopy (FTIR) measurements (supplementary material, Figure S8) of powders were performed. Vibration modes at 850 cm^{-1} in all three materials are associated with Mn−O, Fe−O, and Co−O vibrations [62,74]. Vibration modes between 1300 and 1600 cm^{-1} indicate the presence of organic residues on the surface after SFS. The vibrations in LMO and LFO samples at 1372 and 1479 cm^{-1} are related to the C−H vibration modes [75,76], while additional

vibrations only noticed in LMO at 1420 and 1578 cm^{-1} are attributed to C−H and C=C bonds [77]. Vibrational modes in LCO appear at 1315, 1420, and 1530 cm^{-1}, corresponding to O−C=O, O−H, and C=C vibrations [75,76]. Above 3000 cm^{-1}, it is noted that LMO and LFO possess a significantly higher amount of surface O−H groups than the LCO particles, which correlates perfectly with the HSP data [75].

Based on the HSP, ethanol was found as a suitable continuous phase for dispersing the three perovskites and was selected as the solvent for the subsequent ink formulation. However, ethanol is a common solvent used in various applications and industrial processes, resulting in a massive demand, which has led to increased prices over the last few years [78,79]. Lowering production costs can be achieved by introducing water into the system [79–84]. In contrast to inks solely based on ethanol, the use of water/alcohol mixtures has been observed to impede crack formation and the occurrence of film delamination during drying, mainly stemming from the rapid evaporation of ethanol at elevated temperatures [85,86]. Therefore, stability characterization of the catalysts in ethanol, water, and various mixtures of water/ethanol (50/50, 75/25, and 90/10 v/v%) was conducted (supplementary material, Figure S9–S11). Results for all three perovskites show a similar trend, where the stability of dispersions decreases and material sedimentation accelerates with increasing water concentration. According to the results on dispersion stability, a water/ethanol mixture of 75/25 v/v% is selected as the continuous phase for further formulations, as it presents a good compromise between costs and stability (Figure 3a–c).

Upon selecting the suitable solvent, inks were formulated by the incorporation of Sustainion® as a binder. Our previous findings indicate that incorporating fluorine-free Sustainion® instead of the well-established perfluorinated Nafion® in the electrode preparation of $La_{0.8}Sr_{0.2}CoO_3$ and $NiFe_2O_4$ nanomaterials significantly improves electrode durability, thereby enhancing their performance in the OER [33]. As demonstrated in all cases (Figure 3d–f), the addition of Sustainion® in small concentrations improved the ink stability, resulting in decreased

sedimentation over time. Altogether, we believe that this structured process for ink development and improvement will play an important role for a reproducible electrode fabrication during scale-up.

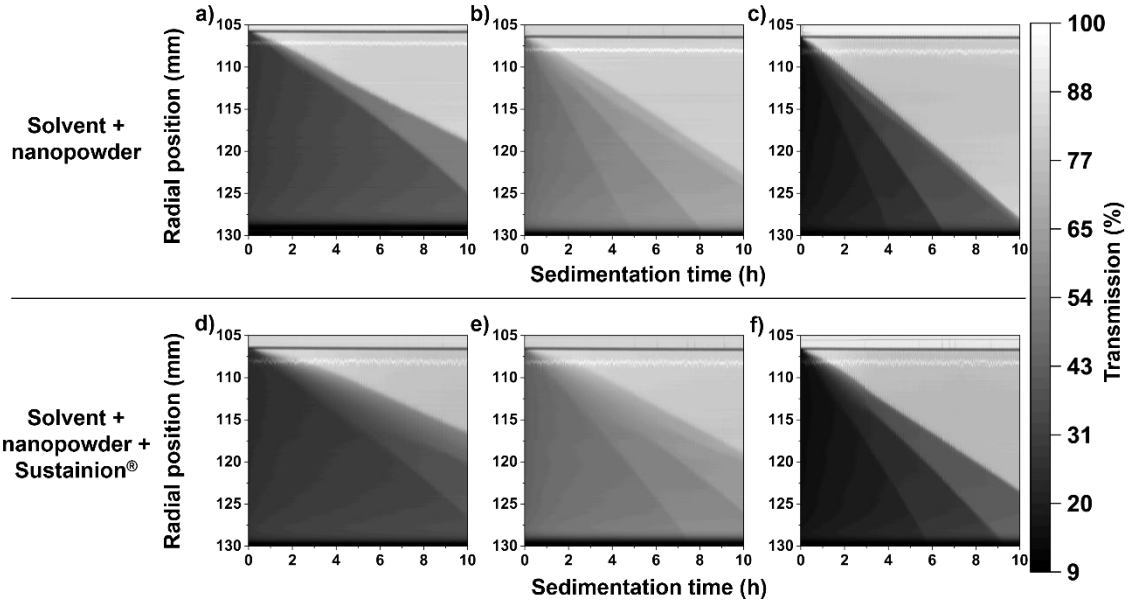

Figure 3. (a-c) Transmittograms of LMO, LFO, and LCO dispersions in H_2O/EtOH 75/25 v/v%. (d-f) Transmittograms of LMO, LFO, and LCO inks with Sustainion® binder in H_2O/EtOH 75/25 v/v%. Darker colors present low transmission and better phase stability over time.

3.3. Structural characterization of catalyst-coated nickel-substrate anodes

The surface morphology and roughness of the LMO-, LFO-, and LCO-based thin-film electrodes were assessed using a SEM, EDX, and AFM. The SEM measurements (Figure 4a–c) confirm that all three electrodes exhibit smooth and slightly porous structures, while EDX analysis indicates uniform elemental distribution across all electrodes. This includes the organic component from the Sustainion® binder (supplementary material, Figure S12–S14), indicating good dispersibility in a water/ethanol environment. Furthermore, AFM (Figure 4d–f) was employed to analyze surface characteristics represented by the square mean root roughness (Sq) values. The *S*q values assessed for LMO-, LFO-, and LCO-based electrodes are situated

between 155 – 180, 160 – 200, and 180 – 220 nm, respectively. The slight rise in surface roughness can be attributed to the increased size of perovskite nanoparticles from LMO towards LCO, as confirmed by TEM and BET analysis. The increase in particle size can also explain the increase in pore surface coverage and average pore size distribution from LMO towards LCO (Table 1**,** supplementary material, Figure S15–S16), as evaluated by the procedure developed by Odungat et al. [87]. It is worth noting that surface roughness and porosity affect the presence of active sites, mass transport, and catalytic performance [32,88–90]. Therefore, additional contact angle measurements were performed (supplementary material, Figure S17), where no significant differences were observed, underpinning constant wetting properties across all three anode materials.

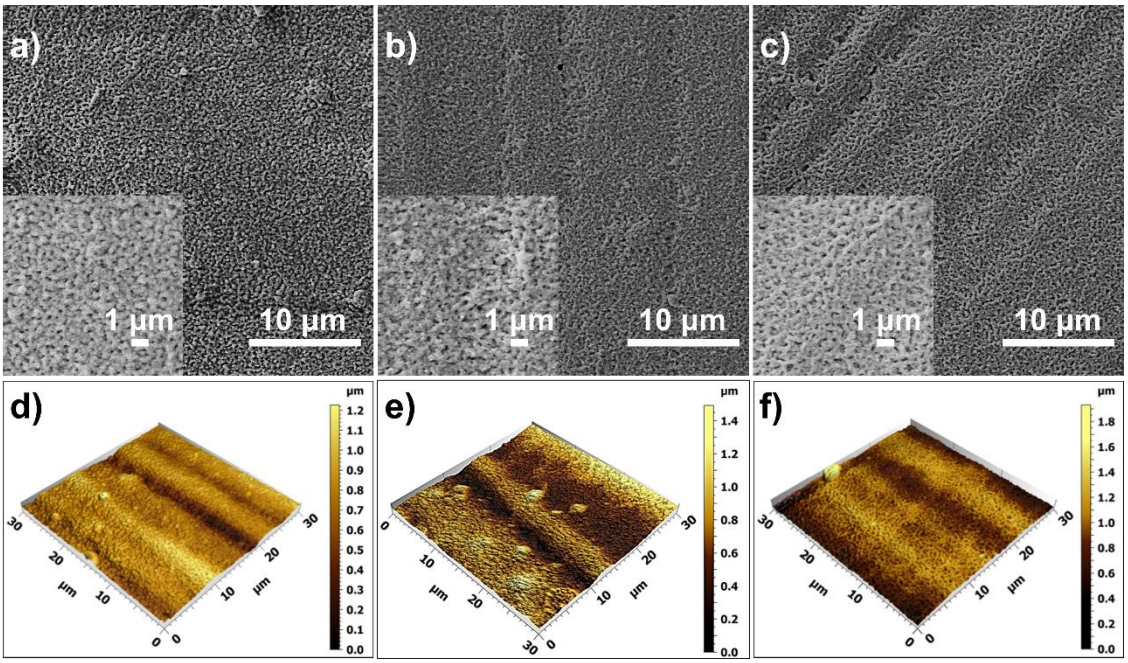

Figure 4. (a-c) SEM images of electrodes made by spray-coating of Sustainion®-containing LMO-, LFO-, and LCO-based inks on nickel substrates. (d-f) AFM topography images of LMO-, LFO-, and LCO-based electrodes.

Table 1 presents the most important parameters for OER. Taking into account the powder synthesis and electrode engineering of our catalysts (including ink formulation, electrode

fabrication, and surface characterization), we can conclude that our methodology enables fast, reproducible, and scalable electrode manufacturing with comparable characteristics. This enables to connect the OER performance primarily to intrinsic properties of the active material, rather than to the structure-driven electrolyte wettability.

The prepared electrodes will be electrochemically evaluated in the next sections using different electrochemical techniques to investigate how the combination of intrinsic material and electrode properties affects the OER performance.

Table 1. Powder and electrode parameters relevant for the OER performance.

Nanopowder parameters			
x_p^{BET} / nm	8.7	9.6	10.0
BET / $m^2\ g^{-1}$	105.2	94.2	84.6
XPS / [$O_{surface}$ /$O_{lattice}$]	0.83	0.94	0.90
HSP			
$\delta_D/\delta_P/\delta_H/R$ / $Mpa^{0.5}$	16.5/10.7/15.0/5.1	16.5/10.7/15.0/5.1	17.1/12.6/14.9/6.6
Electrode parameters			
Sq roughness / nm	155 – 180	160 – 200	180 – 220
Surface pore coverage / %	8.6	8.8	10.6
Contact angle / °	85	89	91

3.4. Electrochemical characterization of catalyst-coated electrodes

3.4.1. Electrochemical testing using scanning droplet cell tests

The lateral homogeneity of the 1 × 1 cm^2 nickel (Ni)-plates coated with 250 µg cm^{-2} LMO, LFO, and LCO with Sustainion® as a binder was assessed by SDC analysis (supplementary

material, Figure S18). For each coated electrode, the electrocatalytic activity was evaluated based on 25 measured areas that were analyzed and spaced 1.8 mm apart (supplementary material, Figure S19, spot area of 0.0021 ± 0.0002 cm^2). Figure S20 (supplementary material) presents the average and standard deviation of the LSVs. LFO-based electrodes exhibit the lowest overpotential value (η) for OER at 10 mA cm^{-2} (1.541 ± 0.002 V vs. RHE) of the investigated catalyst-coated electrodes. At the same current density, the LCO-based electrodes follow with an inferior activity (1.560 ± 0.003 V vs. RHE), while the lowest activity among the coated electrodes is observed for the LMO-based electrodes (1.635 ± 0.007 V vs. RHE). The differences in overpotential among the electrodes were statistically significant ($p < 0.05$).

The role of the homogeneity of the coatings for the OER activity is also represented in the activity maps (supplementary material, Figure S21a–b). The current densities of the 25 individual measured areas of each coated electrode, along with their relative standard deviation compared to the average of the sample across the spots, are represented at a potential of 1.541 V vs. RHE. LFO-based electrodes (8.8 mA cm^{-2}) exhibited a superior average current density compared to LCO-based electrodes (7.4 mA cm^{-2}), and lastly, to the LMO-based electrodes (4.9 mA cm^{-2}). The homogeneity of the OER activity is also evident in the standard deviations of ±16.4, ±11.6, and ±7.6 % of LMO-, LFO-, and LCO-based electrodes, along with their respective maximum deviations of 42.1, 25.6, and 16.3 %, respectively. Despite the coated films appearing visually homogeneous before the SDC measurements (supplementary material, Figure S22), the LMO-based electrode surface was more damaged after the measurements due to the additional force needed to seal the SDC and prevent electrolyte leakage. This result aligns with previous reports indicating that LMO exhibits less activity compared to LCO and $LaMn_xCo_yO_3$-based perovskites [91,92].

In brief, the homogeneity of electrochemical activity for OER was successfully investigated using high-throughput SDC. This automated, versatile, and efficient technique enables precise screening of electrode surfaces, thus providing preliminary data to support and accelerate the

development and scaling-up of new electrocatalysts. However, at this point, the superior performance of the LFO-based electrodes compared to LCO- and LMO-based electrodes raises additional questions, which are discussed in the next section.

3.4.2. Electrochemical half-cell testing using a rotating disc electrode, a compression cell, and a flow cell coupled with ICP-OES

For successful scale-up, accurately determining the electrocatalytic activity is essential for identifying promising candidates and discarding materials with insufficient performance. Electrochemical evaluation typically includes RDE measurements (supplementary material, Figure S23), with glassy carbon (GC) being the most commonly used support material. This is often followed by tests on three-dimensional (3D) metal-based supports, such as Ni foam [33]. As highlighted in previous studies, an important consideration is the potential impact of catalyst–support interactions, which can significantly influence the catalytic performance [93–95]. Furthermore, in our previous study, we proved that the enhanced OER activity on Ni-supported catalysts is associated with the increased contribution of the lattice oxygen mechanism (LOM), while the reaction on GC predominantly follows an adsorbate evolution mechanism (AEM) [95]. To investigate this further, we performed electrochemical measurements in the RDE system using both GC and Ni as support materials, where the induced rotation reduced mass transport limitations and facilitated oxygen bubble removal [96]. Figure 5a-b presents the activity of LFO, LCO, and LMO deposited on a GC and Ni electrode support in a conventional RDE system. The observed trends were similar for both systems, except for the LMO-based electrode, which showed no electrocatalytic activity when GC was used as the support material. In general, the potential values recorded at 10 mA cm^{-2} showed higher overpotentials when the GC was employed as the support, indicating less favorable interfacial charge-transfer kinetics. Our results are further confirmed by plotting the iR-uncorrected LSVs

and by plots of the OER activity as a function of geometric area, ECSA, and mass loading (supplementary material, Figure S24-S27).

Subsequently, EIS measurements were conducted at a potential of 1.6 V vs. RHE to gain further insight into the electrochemical behavior, as shown in Figure S28 (supplementary material). The Nyquist plot revealed significant differences in the charge-transfer resistance (R_{ct}) based on the capacitive arc diameter. For instance, the LFO-based electrode exhibited $R_{ct} \approx 6\ \Omega$ for Ni-coated electrodes and 235 Ω for GC-coated electrodes, highlighting the critical role of the Ni support in facilitating interfacial charge-transfer. The higher R_{ct} observed for GC can be attributed to the absence of complementary catalyst–support interactions, consistent with the reduced OER activity on this support material [95].

Notably, for the LCO-based electrode, two distinct capacitive arcs were observed, indicating two processes with different time constants at the catalyst layer/electrode interface, due to differences in capacitive and resistive properties when Ni is used as the support electrode [97]. This second time constant is evident in the Bode plot (supplementary material, Figure S29a–b), which shows two peaks at approximately 3000 and 10 Hz. The additional interface may affect the electrocatalytic activity by facilitating electron transfer from the catalyst to the electrode or by charging the interface through charge accumulation. In contrast, the LFO- and LMO-based electrodes exhibit a single time constant.

Furthermore, enhanced catalytic activity of LFO-based catalysts in direct contact with Ni has been reported for methane reforming, where the improvement was attributed to strong metal–support interactions (SMSI) that promote Ni–Fe interactions at the catalyst–support interface [98,99]. Such Ni–Fe interactions are well known to induce synergistic effects, leading to modified redox properties and faster reaction kinetics compared to pure Ni or Fe systems, which are also highly active for the OER [100–102].

Beyond interfacial charge-transfer effects, the superior intrinsic OER performance of the LFO-based electrode is further supported by prior density functional theory calculations. Tripkovic

et al. [103] correlated higher overpotential of LCO to changes related to the valence state of the metal center and differences in the number of hydroxyl species on the surface. This is experimentally validated with our XPS results, where the LFO shows the highest hydroxyl group surface coverage ratio (Table 1).

The compression cell (supplementary material, Figure S30) enables the exposure of the electrode surface area to the electrolyte under uniform potential distribution across the exposed area [104]. During measurements, oxygen is not removed and remains in the close vicinity of the electrode [33]. LSV measurements (supplementary material, Figure S31) of electrocatalysts at 10 mA cm^{-2} revealed that the LFO-based electrodes demonstrated the best performance, achieving 1.54 V vs. RHE, closely followed by the LCO-based electrodes with 1.57 V vs. RHE, aligning well with the SDC results. In contrast, the LMO-based catalyst performed significantly worse, with a value of 1.73 V vs. RHE, compared to the other two materials. This is partially attributed to the electrochemically active surface area (ECSA, supplementary material, Figure S32a–d, Table S2–S3), which is significantly lower compared to LFO- and LCO-based electrodes (0.30, 0.57, and 0.55 cm^2). Due to the porous electrode architecture and the material's multimetallic nature, accurately quantifying the number of active sites and, consequently, reliably determining the turnover frequency (TOF) is not feasible [105]. Estimating TOF would require several assumptions. Therefore, ECSA values derived from double-layer capacitance (C_{dl}) measurements were employed to assess and compare the intrinsic catalytic activity.

After approximately 41 mA cm^{-2}, a crossover point in the LSV-curves of the LFO- and LCO-based electrodes is observed. This could be attributed to two possible scenarios. The first is related to the configuration of the electrochemical cell, and the second is connected to material segregation in the LCO-based electrodes [106]. These hypotheses will be evaluated in the following through post-mortem analysis following long-term stability testing. Subsequent chronopotentiometric stability (CP) measurements (Figure 5c) were performed at 10 mA cm^{-2} for 12 h. The same trend was noted from the LSV across the whole measurement window.

During the measurement period, LFO-, LCO-, and LMO-based electrodes showed a slight increase from their initial potential to 1.56, 1.59, and 1.85 V vs. RHE, respectively. Furthermore, low standard deviations of LFO- and LCO-based electrodes suggest good reproducibility of these electrodes under laboratory conditions.

Following the compression cell measurements, post-mortem morphological and elemental evaluations were conducted using EDX, SEM, and AFM. The EDX analysis (supplementary material, Figure S33–S35) exhibits uniform elemental distribution. SEM images (supplementary material, Figure S36a–c) reveal that all electrodes maintain a homogeneous coating after their exposure to the electrochemical treatment, with some randomly allocated agglomerates. However, in the case of LCO-based electrodes, surface cracks are observed post-electrochemical testing. The AFM analysis (supplementary material, Figure S36d-f), conducted after stability testing for 12 h, shows a reduction in the Sq values, while the trend among different materials remains as observed in the case of the pristine electrodes. Among the electrocatalysts, LMO-based electrodes exhibit the smoothest surface with minimal variations across the area. The Sq values range between 85 – 95 nm, followed by LFO-based electrodes, with Sq values between 110 –130 nm. The LCO-based electrodes display the highest Sq values, ranging from 140 – 180 nm, respectively. Similarly to the SEM, AFM also revealed cracks on the surface of LCO-based electrodes, indicating and supporting the hypothesis of material segregation deduced from the crossing of the LSV curves in Figure S31 (supplementary material). This hypothesis was further examined by adhesion testing using the method of centrifugal detachment (supplementary material, Figure S37), which revealed no significant difference between pristine and electrochemically treated electrodes. This indicates that although surface cracking occurs, the overall adhesion of the perovskite nanoparticles to the nickel substrate remains unaffected. Moreover, grazing-incidence X-ray diffraction (GIXRD) was employed to investigate the potential changes in the crystal phase after compression cell measurements (12 h at 10 mA cm^{-2}). While GIXRD (supplementary material, Figure S38) did

not reveal any significant phase changes in LMO-, LFO-, and LCO-based electrodes after electrochemical stress, the strong diffraction signals from the nickel substrate likely masked subtle structural modifications in the perovskite phases, potentially limiting the detection of minor phase transformations.

Finally, the correlation between the methods was evaluated by plotting the overpotential at 10 mA cm^{-2} and comparing the results across the different techniques in Figure S39 (supplementary material). There, one can see that the methods are well correlated. The slight difference observed emerges from the differences in the experimental setups and mass transport conditions. For instance, SDC operates in a regime where no significant amount of gas is evolved, as bubble formation would otherwise block the electrodes due to the cell design [107,108]. In RDE, electrode preparation was via drop-casting. Furthermore, it is a hydrodynamic method in which the solution continuously flows toward the electrode, assisted by electrode rotation, which facilitates bubble detachment and enhances convective mass transport [107,109,110]. On the other hand, in the compression cell, the detachment of the bubbles proceeds by overcoming the adhesive forces between the bubbles and the electrode surface (buoyancy) [109]. Furthermore, the compression cell exposed good structural stability of all La-based electrodes, which is crucial before subjecting the materials to harsher conditions, as unstable materials should not be considered for further testing under application conditions [33].

Integrating the electrochemical cell with ICP-OES (supplementary material, Figure S40) enables the direct analysis of reaction products and establishes a link between dissolution behavior and the electrochemical operation [111]. The configuration plays a vital role in regulating transport processes, including diffusion, convection, and migration of reactive products and bubbles away from the electrode. Additionally, it introduces mechanical stress on the electrode surface, facilitating the investigation of the electrochemical stability [112].

During these measurements, a minor transient of Fe and Mn dissolution (supplementary material, Figure S41a) is observed, independent of the applied potential. The leaching behavior of the metal ions is summarized in Figure S41b (supplementary material). During OER operation, Fe and Mn dissolution are detectable at a current density of 5 and 10 mA cm^{-2}, resulting in approximately 0.25 ng s^{-1} cm^{-2} for Fe and 0.68 ng s^{-1} cm^{-2} for Mn. The dissolution rate of Fe increases transiently and slowly decreases until the end of the hold. The calculated dissolution should be treated with caution under these operating conditions, as it is below the nominal detection limit of the online ICP-OES system (limit of detection for Fe, <10 ppb). However, manganese leaching may be a partial reason for the poor electrochemical performance of LMO-based electrodes, as discussed previously during RDE measurements. Furthermore, no La or Co dissolutions are observed during OER operation at steady-state current.

In conclusion, the OER performance of perovskite catalysts was systematically evaluated using three different complementary lab-scale electrochemical techniques, providing in-depth insights into their performance at low current densities. The findings are in good agreement with the previously used SDC technique. Our results are in sharp contrast to the previously mentioned studies from the literature, which identified LCO powder as the most effective electrocatalyst. However, perovskites in those studies were obtained from different synthesis techniques [18–20]. This deviation suggests that the superior performance of the LFO-based electrode may be attributed first to the distinctive intrinsic properties of the spray-flame synthesized material that provides only minute amounts of organic residuals at the surface, and second, to advanced electrode engineering that enables comparable anodes with only slight variations in the electrode microstructure, which have not been reported before. Although the LMO-based electrodes exhibited substantially higher overpotential, making it less promising, it will still be examined further under application-relevant conditions for a more comprehensive assessment of its capabilities.

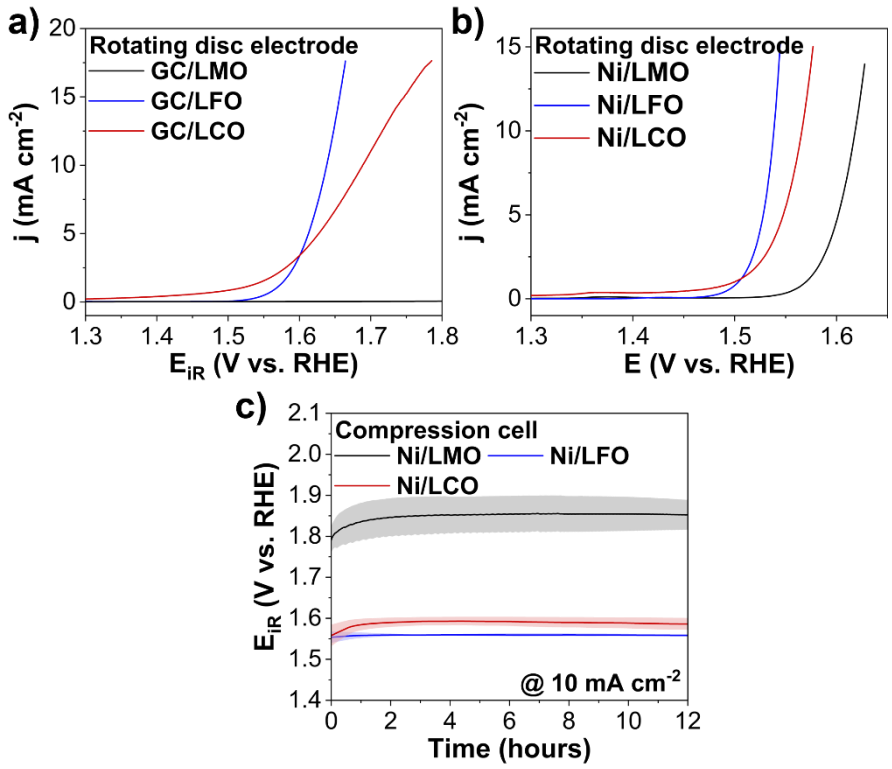

Figure 5. (a, b) LSV curves of LMO- (black), LFO- (blue), and LCO-based electrodes (red) with Sustainion® obtained with the RDE (1600 rpm, O_2-saturated, purified 1 mol L^{-1} KOH) on glassy-carbon and nickel substrate. The shift to lower overpotentials is related to the conductivity of the substrate material. CP measurements were recorded with the compression cell in a purified, O_2-saturated, 1 mol L^{-1} KOH solution. (c) The solid lines represent the mean values, and the shadows indicate their standard deviations.

3.4.3. Electrochemical testing using zero-gap full-cell

Next, anode-testing based on the coherent workflow transitions to the scalable zero-gap full-cell setup (supplementary material, Figure S42) with a membrane electrode assembly (MEA), marking a significant step toward industrial applicability. In our previous study, we highlighted that polarization curves (equivalent to the LSV curves in the half-cell) and long-term stabilities at high current densities are key indicators of whether the combination of catalytic material, binder, and substrate is suitable for future development toward real-life applications [33,113]. Two trends are noticed in the polarization curves. The first one at 500 mA cm^{-2} indicates that

the polarization curves (Table 1, supplementary material, Figure S43a-d) mainly follow the trend noticed with the electrochemical standard laboratory half-cell electrochemical setups. The most significant difference is observed in the polarization curves obtained after 36 h of electrochemical testing, where the LCO-based electrodes, for the first time, outperform the LFO-based electrodes (supplementary material, Figure S43d). Second, the polarization curves of the LMO-based electrodes are much closer to the LCO- and LFO-based electrodes, indicating that the LMO-based anodes under application-relevant conditions show enhanced performance compared to the results gained at 10 mA cm^{-2}. Long-term stability CP measurements (

Figure **6**) were obtained at a current density of 500 mA cm^{-2} for 12 h at room temperature and additionally for 24 h at 60 °C. After exposure for 12 h at room temperature, the cell potential (U_{cell}) of LMO- (2.32 V) and LCO-based electrodes (2.20 V) is relatively stable. In contrast, in the case of LFO-based electrodes (2.17 V), a significant increase in the potential is recorded. This further confirms that the overpotential of LMO-based electrodes during application-relevant conditions is significantly closer to the other two electrocatalysts than suggested by electrochemical half-cell testing.

Furthermore, to simulate real-life electrolyzer conditions more accurately, additional full-cell tests were conducted at 60 °C. In all cases, the elevated temperature led to a significant improvement in U_{cell}. The most substantial decrease in U_{cell} is observed with LMO-based electrodes (0.28 V) compared to the U_{cell} after testing at room temperature, followed by LFO- and LCO-based electrodes with 0.24 and 0.22 V, respectively. Similarly to room temperature measurements, the LFO-based electrodes again show the highest increase of the U_{cell} with time (0.15 V), followed by LMO- (0.12 V) and LCO-based electrodes (0.09 V), aligning with the trends observed in the polarization curves. After 36 h exposure, the LCO-based electrodes show lower U_{cell} compared to LFO- and LMO-based electrodes (2.07, 2.09, and 2.16 V, respectively). This leads to a couple of conclusions. Firstly, close to realistic conditions, all three perovskite electrocatalysts exhibit promising OER performance, including the LMO-based electrodes,

which would typically be discarded after lab testing. Secondly, after 36 h, all electrocatalysts reach a plateau, indicating a steady state of the system. Thirdly, the curve-crossing trends observed between LFO- and LCO-based electrodes point towards material changes that are only evident under harsh conditions and are unknown to standard laboratory electrochemical testing. These changes will be investigated in the post-mortem analysis section.

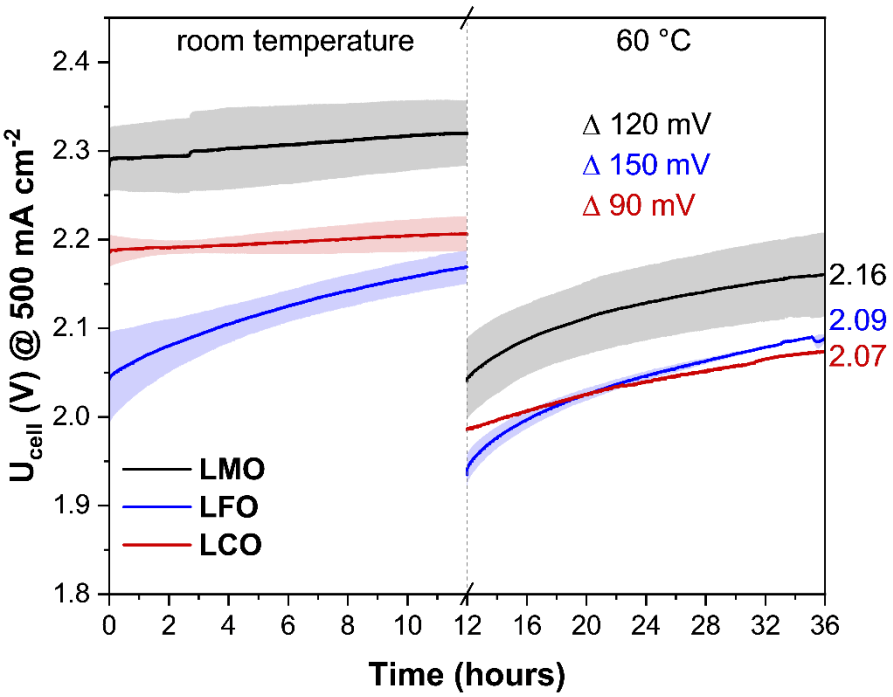

Figure 6. Zero-gap full-cell characterization of LMO- (black), LFO- (blue), and LCO-based electrodes (red) at room temperature and 60 °C at 500 mA cm^{-2} in as-prepared 1 mol L^{-1} KOH on Ni foam substrates.

Table 2. Electrochemical results on the three perovskites gained by electrochemical half-cell-testing at 10 mA cm^{-2} in purified, O_2-saturated, 1 mol L^{-1} KOH. Results are obtained using a zero-gap full-cell at 0.5 A cm^{-2} in as-prepared 1 mol L^{-1} KOH at room temperature and 60 °C.

	LMO / V vs. RHE	LFO / V vs. RHE	LCO / V vs. RHE
SDC / 10 mA cm^{-2}	1.635 ± 0.007	1.541 ± 0.002	1.560 ± 0.003
RDE/GC / 10 mA cm^{-2}	/	1.64	1.69
RDE/Ni / 10 mA cm^{-2}	1.62	1.54	1.57
Compression cell / 10 mA cm^{-2}	1.731 ± 0.007	1.54 ± 0.01	1.566 ± 0.004
	voltage / V	voltage / V	voltage / V
Zero-gap full-cell before CP at room temperature / 0.5 A cm^{-2}	2.27 ± 0.05	1.96 ± 0.09	2.14 ± 0.01
Zero-gap full-cell after CP at room temperature / 0.5 A cm^{-2}	2.23 ± 0.04	2.04 ± 0.03	2.15 ± 0.02
Zero-gap full-cell before CP at 60 °C / 0.5 A cm^{-2}	2.00 ± 0.03	1.86 ± 0.02	1.94 ± 0.05
Zero-gap full-cell after CP at 60 °C / 0.5 A cm^{-2}	2.08 ± 0.05	2.018 ± 0.002	1.97 ± 0.05

3.5. OER mechanism pathway

To gain a deeper insight into the performance changes, post-mortem analysis of the anodes after full-cell testing at room temperature and 60 °C was conducted using Raman spectroscopy, XPS, and GIXRD, complemented by EDX, SEM, and cyclic voltammetry. The results were compared to pristine electrodes that were not exposed to electrochemical conditions, allowing direct correlation between catalytic performance and structural evolution. Together with the

electrochemical data, this provides a comprehensive understanding of the materials' behavior under realistic operating conditions.

Raman spectroscopy of LMO-based electrodes (Figure 7a) reveals two vibrational modes at 498 and 616 cm^{-1}, corresponding to Jahn–Teller distortion in MnO_6 octahedra [45,46]. After full-cell testing at room temperature, the spectra remain nearly unchanged compared to the pristine electrode. However, following the operation at 60 °C, a new band emerges at 572 cm^{-1}, assigned to Mn–O stretching vibrations and increased presence of Mn^{4+} [114,115]. XPS confirms these observations, with the Mn $2p_{3/2}$ peak shifting toward higher values from 641.6 eV in the pristine sample to 642.1 eV after 36 h testing (Figure 8a), being consistent with Raman spectroscopy observations [116,117]. The O 1s spectra **(**Figure 8b) further reveal a reduction of lattice oxygen and an increase in surface oxygen species [118], while the La $3d_{5/2}$ multiplet splitting (supplementary material, Figure S44a) remains constant at 3.7 eV [52,53]. Additionally, GIXRD measurements (supplementary material, Figure S45a) reveal no detectable structural degradation, indicating that the LMO lattice retains long-range order. The mechanistic link to catalytic performance is further clarified by the CV data obtained with the compression cell (supplementary material, Figure S46a), which displays anodic and cathodic peaks at 1.36 and 1.28 V vs. RHE, respectively, corresponding to the Mn^{3+}/Mn^{4+} and Mn^{4+}/Mn^{3+} transitions. The enrichment of Mn^{4+} detected by Raman and XPS aligns directly with these redox transitions and previous reports [55]. Charge compensation during Mn^{3+} to Mn^{4+} oxidation proceeds via oxygen loss from the MnO_6 octahedra, facilitating the generation of reactive oxygen species [9]. Thus, LMO electrodes operate through surface oxidation to Mn^{4+} with a possible participation of lattice oxygen, while retaining bulk structural stability. These observations indicate a likely contribution of LOM during Mn oxidation, occurring alongside conventional AEM pathways.

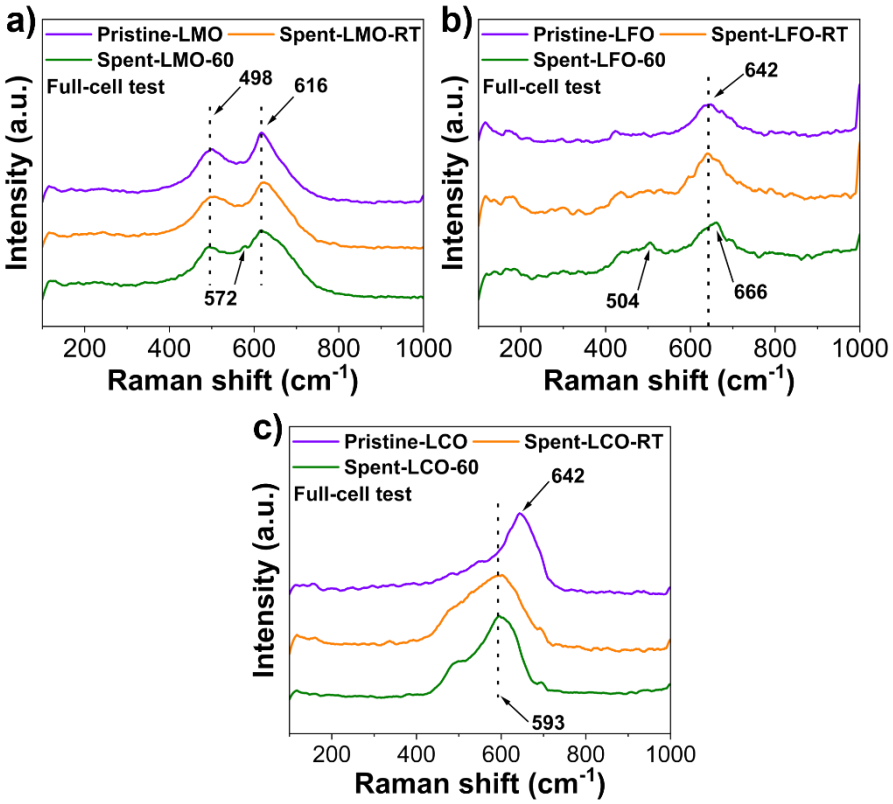

Figure 7. (a, b, and c) Raman spectroscopy data of LMO-, LFO-, and LCO-based electrodes before and after electrochemical testing in a zero-gap full-cell. Measurements were performed on pristine electrodes (magenta) and electrodes after full-cell testing at room temperature (spent-RT, orange) and 60 °C (spent-60, green).

In LFO-based electrodes, Raman spectra (Figure 7b) exhibit a strong band at 642 cm^{-1}, corresponding to FeO_6 stretching vibrations [47,49]. New Raman bands at 504 and 666 cm^{-1} indicate bulk enrichment with Fe^{3+} species [119,120]. Furthermore, EDX mapping revealed surface iron accumulation, which directly correlated with the previously detected Fe leaching by ICP-OES (supplementary material, Figure S47, Table S4). XPS provides complementary evidence, as the La $3d_{5/2}$ multiplet splitting decreases slightly from 3.8 to 3.6 eV (supplementary material, Figure S44b), but remains close to the literature-reported value of 3.7 eV [52,53]. The Fe $2p_{3/2}$ region exhibits a new peak at 713.7 eV (Figure 8c), indicating the formation of a thin layer of Fe^{4+} [121]. Consistent with this, the O 1s spectra (Figure 8d) show a reduction in lattice

oxygen and an increase in adsorbed oxygen species. Contact angle measurements on LFO-based electrodes (supplementary material, Figure S48) showed no significant change before and after electrochemical operation, indicating that the wettability remained stable and is therefore unlikely to influence the OER performance, regardless of the surface Fe^{4+} enrichment. GIXRD (supplementary material, Figure S45b) confirms that these modifications are restricted to the surface, as no bulk structural changes are observed. CV analysis (supplementary material, Figure S46b) reveals an anodic peak at 1.44 V vs. RHE, assigned to the Fe^{3+}/Fe^{4+} transition [122]. The intensity of this peak increases during extended cycling, consistent with the detection of Fe^{4+} by XPS. However, the cathodic peaks shift to lower potentials, reflecting sluggish reduction kinetics from Fe^{4+} to Fe^{3+}. A slow redox transition may limit the formation of reactive oxygen species on the surface and contributes to the potential increase observed under long-term, high-current operation [123]. The combined spectroscopic and electrochemical evidence demonstrates that surface Fe oxidation, partial dissolution, and slow redox cycling dictate the moderate activity and limited stability of LFO electrodes under industry-relevant conditions. The sluggish Fe^{3+}/Fe^{4+} redox kinetics and limited participation of lattice oxygen indicate a predominantly AEM, with a minor contribution from the LOM.

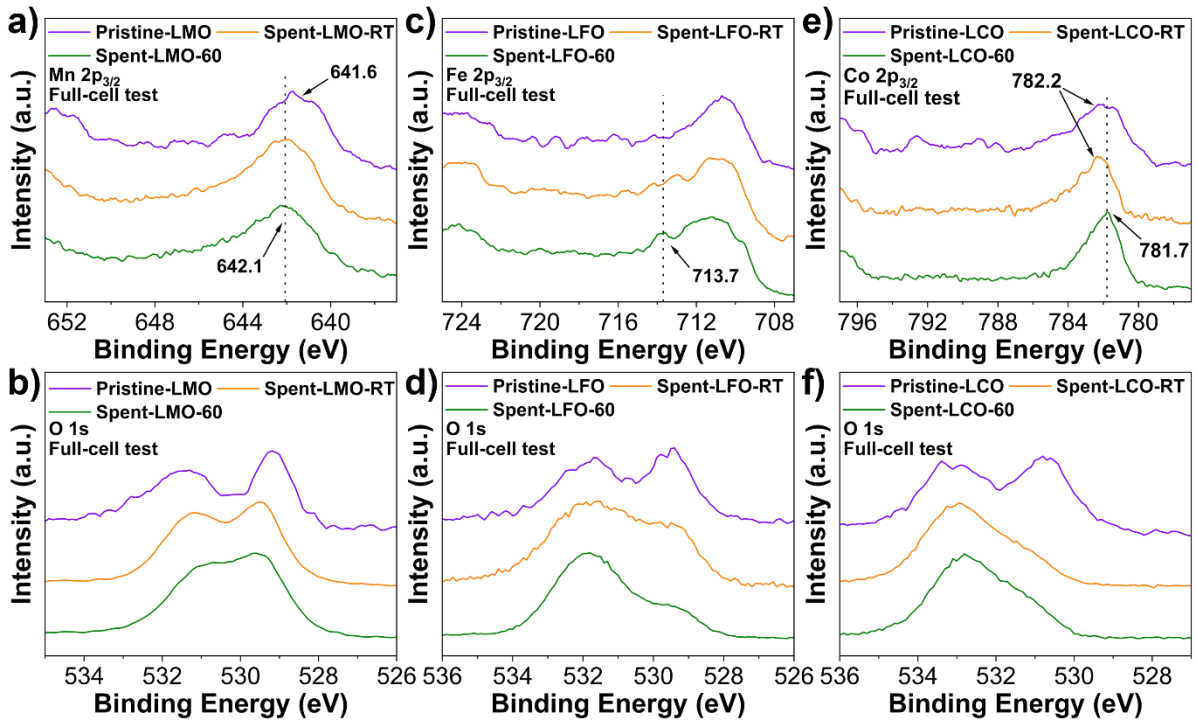

Figure 8. (a, b) XPS data of Mn $2p_{3/2}$ and O1s on LMO-based electrodes. (c, d) XPS data of Fe $2p_{3/2}$ and O 1s on LFO-based electrodes. (e,f) XPS data of Co $2p_{3/2}$ and O1s on LCO-based electrodes. Measurements are performed on pristine perovskite electrodes (magenta) and electrodes after full-cell testing at room temperature (spent-RT, orange) and at 60 °C (spent-60, green). All materials were exposed to a current density of 500 mA cm^{-2}.

In contrast, LCO-based electrodes undergo more pronounced restructuring. Raman spectra of the pristine material exhibit a Co–O stretching mode at 642 cm^{-1} [50,51]. After testing at 0.5 A cm^{-2}, this band shifts by 49 cm^{-1} to 593 cm^{-1}, indicating partial Co dissolution and the formation of amorphous $CoO_x(OH)_y$ (Figure 7c). TEM imaging (supplementary material, Figure S49) further confirms the coexistence of crystalline and amorphous domains. Consistent with these observations, XPS supports these findings, showing a decrease in the La $3d_{5/2}$ multiplet splitting from 3.8 to 3.5 eV (supplementary material, Figure S44c). In addition, the Co $2p_{3/2}$ peak shifts from 782.2 to 781.7 eV (Figure 8e), consistent with increased Co^{3+} and $CoO_x(OH)_y$ formation [124,125], while an enhancement of surface oxygen species is observed in the O 1s spectra

(Figure 8f). GIXRD (supplementary material, Figure S45c) indicates lattice expansion after testing at 60 °C, with diffraction peaks shifting to lower 2θ values. The Rietveld refinement reveals an increase in crystallite size by 2.9 ± 1.8 nm and unit cell volume from 341.0 ± 1.3 $Å^3$ to 365.7 ± 1.5 $Å^3$ (supplementary material, Figure S51, Table S5). These results point to preferential dissolution of small crystallites, recrystallization of La-rich phases, and stabilization of a Co-rich amorphous surface. A more detailed explanation of the amorphization process is provided in Section S2.1 (supporting information). Additional mechanistic insight is provided by the supplemental CV analysis (supplementary material, Figure S46c). In the 1st cycle, two anodic peaks appear at 1.33 and 1.39 V vs. RHE, corresponding to the Co^{2+}/Co^{3+} and the Co^{3+}/Co^{4+} transition [126]. With continued cycling, the higher-potential feature progressively diminishes, and by the Co^{2+}/Co^{3+} transition, by the 10th and 50th cycles, it reflects irreversible interfacial reconstruction. Surface modification and reconstruction, driven by the accumulation of Co^{3+} species during anodic activation, facilitate the generation of reactive oxygen species at the surface, thereby enhancing OER catalytic activity and stability [106,125]. This behavior is consistent with Raman, XPS, and GIXRD data and evidence for the formation of a stable amorphous $CoO_x(OH)_y$ layer. The formation of an amorphous $CoO_x(OH)_y$ surface layer and the enhanced abundance of surface oxygen species indicate a strong LOM contribution in addition to AEM [127].

Surface amorphization of Co-species due to dissolution and partial crystallization on top of an initially crystalline catalyst was also previously addressed in the literature [128]. This finding aligns with those of Li et al. [129], who demonstrated that the amorphization of LCO improves the electrocatalyst's activity. Similar studies by Cai et al. [130] and Indra et al. [131] also support the observation that amorphous catalysts exhibit greater stability compared to crystalline structures.

In total, the combined results from post-mortem analyses using Raman spectroscopy, XPS, and GIXRD, after electrochemical half-cell and full-cell testing, reveal a direct link between the

material's electrochemical performance and the observed material properties. Across all three perovskites, redox activity of the B-site cations and the increased abundance of surface oxygen species indicate active surface states formed under anodic polarization. However, the extent of lattice involvement differs with B-site transition-metal composition and the degree of restructuring. LMO shows predominantly surface Mn oxidation while retaining bulk long-range order, suggesting an AEM-dominated pathway with a minor lattice-oxygen contribution during oxidation of Mn^{3+} to Mn^{4+}. LFO exhibits surface Fe oxidation accompanied by partial dissolution and sluggish reduction of Fe^{4+} to Fe^{3+}, consistent with predominantly AEM behavior and limited lattice-oxygen participation. In contrast, LCO undergoes pronounced restructuring toward an amorphous $CoO_x(OH)_y$-rich surface with enhanced surface oxygen species, indicating a stronger lattice-oxygen contribution in addition to AEM. Notably, full-cell testing provides insights into the materials' behavior under realistic operating conditions that are not accessible through half-cell experiments alone. This integrated approach underscores the importance of evaluating electrode stability and reactivity at high current densities.

3.6. Stability under industrially relevant conditions

To simulate real operating environments, degradation testing was performed at 60 °C for 12 h and 100 h under a constant current density of 1000 mA cm^{-2}. Such conditions closely mimic industrial operations, where both high current density and elevated temperature significantly accelerate degradation. The applied protocol, therefore, provides a stringent benchmark for assessing catalytic stability and long-term durability.

Over the 12 h measurement window (Figure 9), LCO-based electrodes exhibit the best overall performance and stability, followed by LFO- and LMO-based electrodes. These results closely resemble those observed at the end of testing at 500 mA cm^{-2}, are further confirmed by the EIS data collected at different current densities (supplementary material, Figure S51-S52), and follow the established literature [132]. In addition, a 100 h degradation study was performed on

LFO-based electrodes (supplementary material, Figure S53), which shows that our perovskites can withstand harsh conditions while maintaining reasonable catalytic performance. It should be noted that periodic sharp increases in potential are associated with daily electrolyte replenishment, while minor signal fluctuations may be due to bubble removal or an unoptimized setup. While these factors represent a current limitation, they simultaneously highlight opportunities for further technical optimization and deeper exploration of perovskite-based materials as potential OER electrocatalysts in full-cell setups.

Overall, degradation tests at 1000 mA cm^{-2} closely followed the previously gathered results. However, the rapid transition from lab testing to industry-relevant scale remains a bottleneck, hindering faster development. Additionally, our perovskites exhibit superior performance compared with previously investigated A- and B-site-substituted perovskites in the zero-gap AEM configuration [4].

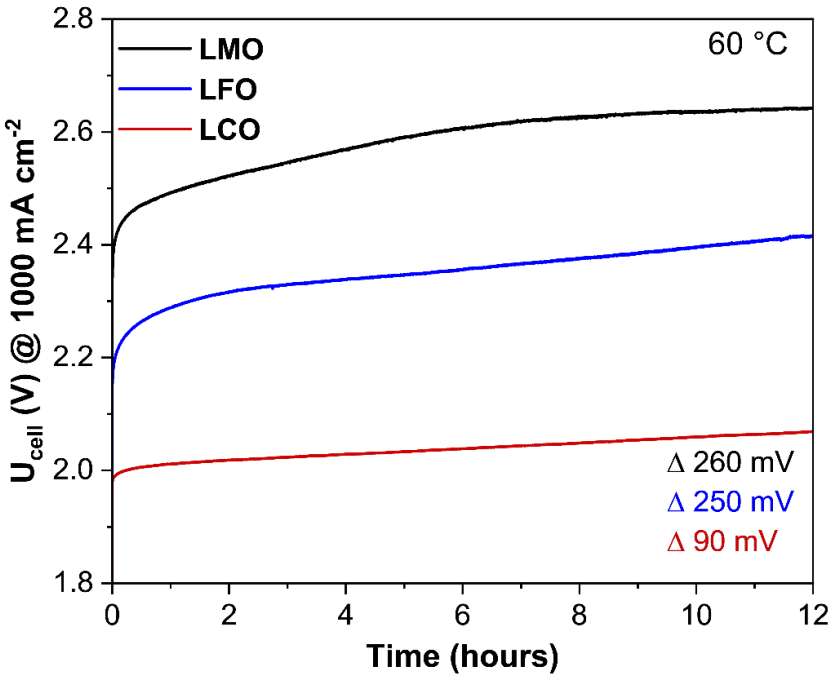

Figure 9. Degradation study in a zero-gap full-cell of LMO- (black), LFO- (blue), and LCO-based electrodes (red) at 60 °C, and 1000 mA cm^{-2} in as-prepared 1 mol L^{-1} KOH on Ni foam substrates.

4. Conclusions

In this research, we investigated the effects of electrode material engineering on OER performance, emphasizing scalable technologies and application-relevant testing. By incorporating a structured, coherent workflow, we demonstrated a comprehensive strategy to evaluate La-based perovskites at different scales. This approach also accelerates knowledge transfer for the future development of next-generation electrocatalysts at relevant scales, which are crucial to alleviating climate change. Based on our investigation, we can conclude:

- Firstly, SFS-synthesized nanopowders possess unique intrinsic properties, including high crystallinity, phase purity, and large specific surface areas exceeding 80 $m^2 g^{-1}$, which make the SFS process a suitable and scalable route for large-scale catalyst production.
- Secondly, optimized ink formulation and controlled structural engineering enabled reproducible electrode fabrication with comparable surface properties, allowing intrinsic material effects to be reliably assessed, without surface-related effects.
- Thirdly, electrochemical half-cell testing highlighted the critical role of substrate selection. In contrast, a zero-gap full-cell at 60 °C and 500 or 1000 mA cm^{-2} revealed the intrinsic catalytic properties of the materials. While LCO-based electrodes exhibited superior stability, LMO- and LFO-based electrocatalysts maintained competitive activity at high current densities, highlighting their potential as toxic-metal-free OER electrocatalysts.
- Fourthly, post-mortem analysis using Raman spectroscopy, XPS, GIXRD, and cyclic voltammetry linked performance to OER mechanisms. In particular, SMSI between the perovskite catalysts and the Ni substrate influences interfacial charge-transfer and redox behavior. The results show that the activity of LMO- and LFO-based anodes is primarily governed by surface oxidation processes proceeding mainly via the AEM, with a minor contribution from the LOM. In contrast, LCO undergoes pronounced surface

reconstruction and amorphization, thereby enabling a greater contribution of LOM alongside AEM, ultimately leading to superior long-term electrochemical stability.

Altogether, our findings contribute to the systematic exploration of perovskite-based OER electrocatalysts by integrating full-cell testing into the material assessment process. We believe that these studies are necessary to gain a holistic understanding of electrocatalysts and enable bridging the gap between academia and industry. Notably, our results highlight the potential of gas-phase-synthesized perovskites using non-toxic, earth-abundant transitional metals such as iron and manganese. However, further improvements in catalytic stability and a deeper understanding of substrate effects are still required to optimize electrode design and complete the picture of effective electrode development for efficient alkaline water electrolysis.

CRediT authorship contribution statement

Blaž Toplak: Writing – original draft, Investigation, Formal analysis, Conceptualization. **Leon Müller:** Writing – original draft, Investigation, Formal analysis. **Ali Raza Khan:** Investigation, Formal analysis, Writing – review and editing. **André Olean-Oliveira:** Methodology, Conceptualization, Writing – review and editing, Supervision. **Khuzaifa Yahuza Muhammad:** Investigation, Formal analysis, Writing – review and editing. **Wang Feng:** Investigation. **Raíssa Ribeiro Lima Machado:** Investigation, Formal analysis, Writing – review and editing. **Da Xing:** Methodology, Conceptualization, Writing – review and editing, Supervision. **Mohammed-Ali Sheikh:** Investigation, Formal analysis, Writing – review and editing. **Leander Kucklick:** Investigation, Formal analysis, Writing – review and editing. **Ahammed Suhail Odungat:** Investigation, Writing – review and editing. **Adarsh Jain:** Investigation, Writing – review and editing. **Lars Grebener:** Investigation, Writing – review and editing. **Philipp Gerschel:** Methodology, Writing – review and editing, Supervision. **Corina Andronescu:** Funding acquisition, Writing – review and editing, Supervision. **Harry Hoster:**

Funding acquisition, Writing – review and editing, Supervision. **Christof Schulz:** Funding acquisition, Writing – review and editing, Supervision. **Viktor Čolić:** Writing – review and editing, Supervision. **Ulf-Peter Apfel:** Funding acquisition, Writing – review and editing, Supervision. **Hartmut Wiggers:** Funding acquisition, Writing – review and editing, Supervision. **Mohaned Hammad:** Methodology, Writing – review and editing, Supervision. **Doris Segets:** Funding acquisition, Writing – review and editing, Supervision.

Acknowledgments

B. Toplak gratefully acknowledges a scholarship from the International Max Planck Research School (IMPRS) RECHARGE doctoral program. A.R. Khan acknowledges the support of a Ph.D. fellowship awarded by the Higher Education Commission (HEC) of Pakistan and the German Academic Exchange Service (DAAD). K. Yahuza Muhammad. acknowledges Petroleum Technology Development Fund (PTDF), Nigeria, for a doctoral fellowship with Pef No.: PTDF/ED/OSS/PHD/KYM/1723/20 and ID: 20PHD031.The authors acknowledge funding by the German Research Foundation (DFG) within the CRC/TRR 247 (Heterogeneous Oxidation Catalysis in the Liquid Phase 388390466), the Mercator Research Center Ruhr within the DIMENSION project (MERCUR.Exzellenz, 'DIMENSION' Ex-2021-0034). D. Segets, H. Hoster, C. Schulz, C. Andronescu, and U.-P. Apfel would also like to acknowledge the Ministry of Culture and Science of the State of North Rhine-Westphalia (Materials for Future Hydrogen Technologies – Mat4Hy) support. All contributors acknowledge MAT4HY.NRW Consortium for cooperative support. C. Andronescu acknowledges funding by the Ministry of Culture and Science of the State of North Rhine-Westphalia (PB NRW 2022 - Application 19). The authors also gratefully acknowledge the support from the Interdisciplinary Center for Analytics on the Nanoscale (ICAN), a core facility at the University of Duisburg-Essen. The nanopowder X-Ray data were collected using the Panalytical Empyrean at the Institute for Materials Science (UDEMAT). We would like to thank D.C. Lupascu for assistance in using the instrument. The

electrode X-ray data were collected using the Rigaku Smartlab High-Resolution diffractometer of the Nanoparticle Processing Technology (NPPT) group at the University of Duisburg-Essen. The instrument is funded through the DFG Instrument proposal INST 20876/395-1 FUGG project number 450350889 and the state of North Rhine-Westphalia, Germany. We would like to thank M. Schroer for assistance in using the instrument. The authors would also like to thank J. Kleinhaus for his supervision and support during the zero-gap full-cell electrochemical testing.

Declaration of generative AI and AI-assisted technologies in the manuscript preparation process

During the preparation of this work, the authors used ChatGPT to improve readability. After using this tool, the authors reviewed and edited the content as needed and take full responsibility for the content of the published article.

5. References

[1] S. Anantharaj, S.R. Ede, K. Sakthikumar, K. Karthick, S. Mishra, S. Kundu, Recent Trends and Perspectives in Electrochemical Water Splitting with an Emphasis on Sulfide, Selenide, and Phosphide Catalysts of Fe, Co, and Ni: A Review, ACS Catal. 6 (2016) 8069–8097. https://doi.org/10.1021/acscatal.6b02479.

[2] B. Mohanty, P. Bhanja, B.K. Jena, An overview on advances in design and development of materials for electrochemical generation of hydrogen and oxygen, Materials Today Energy 23 (2022) 100902. https://doi.org/10.1016/j.mtener.2021.100902.

[3] F. Liu, R. Hu, H. Qiu, H. Miao, Q. Wang, J. Yuan, Constructing high-activity Cobalt-based Perovskite hybrid by a top-down phase evolution method for the direct seawater electrolysis anode, Journal of Alloys and Compounds 913 (2022) 165342. https://doi.org/10.1016/j.jallcom.2022.165342.

[4] N. Yu, Y. Ma, J.-K. Ren, Z.-J. Zhang, H.-J. Liu, J. Nan, Y.-C. Li, Y.-M. Chai, B. Dong, High negative voltage activating perovskite oxide with bi-vacancy synergistic regulation for water oxidation, Chemical Engineering Journal 478 (2023) 147415. https://doi.org/10.1016/j.cej.2023.147415.

[5] S.A. Chaudhari, V.V. Patil, V.A. Jadhav, P. Thorat, S.S. Sutar, T.D. Dongale, V. Parale, V. Patil, D.S. Mhamane, M.G. Mali, H.-H. Park, Conductivity boosted BiVO 4 for enhanced OER and supercapacitive performance: Stability insights with modeling, predictions, and forecasting using machine learning technique, Energy Mater. 5 (2025). https://doi.org/10.20517/energymater.2024.229.

[6] J. Baek, M.D. Hossain, P. Mukherjee, J. Lee, K.T. Winther, J. Leem, Y. Jiang, W.C. Chueh, M. Bajdich, X. Zheng, Synergistic effects of mixing and strain in high entropy spinel oxides for oxygen evolution reaction, Nat. Commun. 14 (2023) 5936. https://doi.org/10.1038/s41467-023-41359-7.

[7] X. Chen, Z. Zhang, Y. Chen, R. Xu, C. Song, T. Yuan, W. Tang, X. Gao, N. Wang, L. Cui, Research advances in earth-abundant-element-based electrocatalysts for oxygen evolution reaction and oxygen reduction reaction, Energy Mater (2023). https://doi.org/10.20517/energymater.2023.12.

[8] J.X. Flores-Lasluisa, F. Huerta, D. Cazorla-Amorós, E. Morallón, LaNi1-xCoxO3 perovskites for application in electrochemical reactions involving molecular oxygen, Energy 273 (2023) 127256. https://doi.org/10.1016/j.energy.2023.127256.

[9] A. Ashok, A. Kumar, J. Ponraj, S.A. Mansour, F. Tarlochan, Enhancing the electrocatalytic properties of LaMnO3 by tuning surface oxygen deficiency through salt assisted combustion synthesis, Catalysis Today 375 (2021) 484–493. https://doi.org/10.1016/j.cattod.2020.05.065.

[10] M.S. Alom, C.C.W. Kananke-Gamage, F. Ramezanipour, Perovskite Oxides as Electrocatalysts for Hydrogen Evolution Reaction, ACS Omega 7 (2022) 7444–7451. https://doi.org/10.1021/acsomega.1c07203.

[11] J. Suntivich, K.J. May, H.A. Gasteiger, J.B. Goodenough, Y. Shao-Horn, A perovskite oxide optimized for oxygen evolution catalysis from molecular orbital principles, Science 334 (2011) 1383–1385. https://doi.org/10.1126/science.1212858.

[12] J.A. Dias, M.A.S. Andrade, H.L.S. Santos, M.R. Morelli, L.H. Mascaro, Lanthanum-Based Perovskites for Catalytic Oxygen Evolution Reaction, ChemElectroChem 7 (2020) 3173–3192. https://doi.org/10.1002/celc.202000451.

[13] L. Tang, Z. Chen, F. Zuo, B. Hua, H. Zhou, M. Li, J. Li, Y. Sun, Enhancing perovskite electrocatalysis through synergistic functionalization of B-site cation for efficient water splitting, Chemical Engineering Journal 401 (2020) 126082. https://doi.org/10.1016/j.cej.2020.126082.

[14] A. Mendoza, O. Guzmán, Low-Doped Regime Experiments in LaMnO 3 Perovskites by Simultaneous Substitution on Both La and Mn Sites, in: P. Sharma, A. Kumar (Eds.), Recent Advances in Multifunctional Perovskite Materials, IntechOpen, 2022.

[15] J. Chen, M. Shen, X. Wang, G. Qi, J. Wang, W. Li, The influence of nonstoichiometry on LaMnO3 perovskite for catalytic NO oxidation, Applied Catalysis B: Environmental 134-135 (2013) 251–257. https://doi.org/10.1016/j.apcatb.2013.01.027.

[16] Z. Jia, C. Cheng, X. Chen, L. Liu, R. Ding, J. Ye, J. Wang, L. Fu, Y. Cheng, Y. Wu, Applications of all-inorganic perovskites for energy storage, Mater. Adv. 4 (2023) 79–104. https://doi.org/10.1039/D2MA00779G.

[17] Y. Wang, Y. Wang, X. Liu, Y. Guo, Y. Guo, G. Lu, Nanocasted synthesis of the mesostructured LaCoO3 perovskite and its catalytic activity in methane combustion, J. Nanosci. Nanotechnol. 9 (2009) 933–936. https://doi.org/10.1166/jnn.2009.c057.

[18] A. Ashok, A. Kumar, R.R. Bhosale, F. Almomani, S.S. Malik, S. Suslov, F. Tarlochan, Combustion synthesis of bifunctional LaMO3 (M = Cr, Mn, Fe, Co, Ni) perovskites for oxygen reduction and oxygen evolution reaction in alkaline media, Journal of Electroanalytical Chemistry 809 (2018) 22–30. https://doi.org/10.1016/j.jelechem.2017.12.043.

[19] M.V. Kante, M.L. Weber, S. Ni, I.C.G. van den Bosch, E. van der Minne, L. Heymann, L.J. Falling, N. Gauquelin, M. Tsvetanova, D.M. Cunha, G. Koster, F. Gunkel, S. Nemšák, H. Hahn, L. Velasco Estrada, C. Baeumer, A High-Entropy Oxide as High-Activity Electrocatalyst for Water Oxidation, ACS Nano 17 (2023) 5329–5339. https://doi.org/10.1021/acsnano.2c08096.

[20] T.X. Nguyen, Y.-C. Liao, C.-C. Lin, Y.-H. Su, J.-M. Ting, 2021. Advanced High Entropy Perovskite Oxide Electrocatalyst for Oxygen Evolution Reaction. Adv Funct Materials 31, 2101632. https://doi.org/10.1002/adfm.202101632.

[21] R. Xie, Z. Nie, X. Hu, Y. Yu, C. Aruta, N. Yang, Pr-Doped LaCoO 3 toward Stable and Efficient Oxygen Evolution Reaction, ACS Appl. Energy Mater. 4 (2021) 9057–9065. https://doi.org/10.1021/acsaem.1c01348.

[22] J.X. Flores-Lasluisa, F. Huerta, D. Cazorla-Amorós, E. Morallon, Carbon Material and Cobalt-Substitution Effects in the Electrochemical Behavior of LaMnO3 for ORR and OER, Nanomaterials (Basel) 10 (2020). https://doi.org/10.3390/nano10122394.

[23] B. Alkan, S. Cychy, S. Varhade, M. Muhler, C. Schulz, W. Schuhmann, H. Wiggers, C. Andronescu, Spray-Flame-Synthesized LaCo 1− x Fe x O 3 Perovskite Nanoparticles as Electrocatalysts for Water and Ethanol Oxidation, ChemElectroChem 6 (2019) 4266–4274. https://doi.org/10.1002/celc.201900168.

[24] W. Qin, Z. Yuan, H. Gao, R. Zhang, F. Meng, Perovskite-structured LaCoO3 modified ZnO gas sensor and investigation on its gas sensing mechanism by first principle, Sensors and Actuators B: Chemical 341 (2021) 130015. https://doi.org/10.1016/j.snb.2021.130015.

[25] D. Navas, S. Fuentes, A. Castro-Alvarez, E. Chavez-Angel, Review on Sol-Gel Synthesis of Perovskite and Oxide Nanomaterials, Gels 7 (2021). https://doi.org/10.3390/gels7040275.

[26] H. Zhang, B.H.H. Goh, C.T. Chong, Y. Zhang, C.T. Lee, Y. Gao, B. Tian, M.-V. Tran, M.F. Mohd Yasin, J.-H. Ng, A review of flame aerosol synthesis technology for the synthesis of nanoparticles and functional energy materials, Journal of Solid State Chemistry 336 (2024) 124774. https://doi.org/10.1016/j.jssc.2024.124774.

[27] K. Wegner, B. Schimmöller, B. Thiebaut, C. Fernandez, T.N. Rao, Pilot Plants for Industrial Nanoparticle Production by Flame Spray Pyrolysis, KONA 29 (2011) 251–265. https://doi.org/10.14356/kona.2011025.

[28] A.J. Gröhn, S.E. Pratsinis, A. Sánchez-Ferrer, R. Mezzenga, K. Wegner, Scale-up of Nanoparticle Synthesis by Flame Spray Pyrolysis: The High-Temperature Particle Residence Time, Ind. Eng. Chem. Res. 53 (2014) 10734–10742. https://doi.org/10.1021/ie501709s.

[29] C. Dimitriou, P. Psathas, M. Solakidou, Y. Deligiannakis, Advanced Flame Spray Pyrolysis (FSP) Technologies for Engineering Multifunctional Nanostructures and Nanodevices, Nanomaterials (Basel) 13 (2023). https://doi.org/10.3390/nano13233006.

[30] H. Sadabadi, S.R. Allahkaram, A. Kordijazi, O. Akbarzadeh, P.K. Rohatgi, 2021. Structural characterization of LaCoO 3 perovskite nanoparticles synthesized by sol–gel autocombustion method. Engineering Reports 3, e12335. https://doi.org/10.1002/eng2.12335.

[31] L. Grebener, A.S. Odungat, Y. Zhu, O. Pasdag, I. Radev, E. Nürenberg, A. Kubina, V. Peinecke, S. Kohsakowski, D. Segets, F. Özcan, Investigation of fuel cell catalyst dispersion formulations for indirect roll-to-roll fabrication of catalyst coated membranes for proton exchange membrane fuel cells, Journal of Power Sources 635 (2025) 236457. https://doi.org/10.1016/j.jpowsour.2025.236457.

[32] A. Jain, C. Marcks, L. Grebener, J. Johny, A.S. Odungat, M. Chatwani, M.-A. Kräenbring, A. Shaji, M.F. Tesch, A.K. Mechler, V. Vinayakumar, D. Segets, 2025. A Proof-of-Principle Demonstration: Exploring the Effect of Anode Layer Microstructure on the Alkaline Oxygen Evolution Reaction. Adv Funct Materials, 2421352. https://doi.org/10.1002/adfm.202421352.

[33] P. Gerschel, S. Angel, M. Hammad, A. Olean-Oliveira, B. Toplak, V. Chanda, R. Martínez-Hincapié, S. Sanden, A.R. Khan, Da Xing, A.S. Amin, H. Wiggers, H. Hoster, V. Čolić, C. Andronescu, C. Schulz, U.-P. Apfel, D. Segets, 2024. Determining materials for energy conversion across scales: The alkaline oxygen evolution reaction. Carbon Energy, e608. https://doi.org/10.1002/cey2.608.

[34] B. Kirubasankar, J. Kwon, S. Hong, Y.S. Won, S.H. Choi, J. Lee, J.W. Kim, K.K. Kim, S.M. Kim, A robust and highly active bimetallic phosphide/oxide heterostructure electrocatalyst for efficient industrial-scale hydrogen production, Nano Energy 128 (2024) 109805. https://doi.org/10.1016/j.nanoen.2024.109805.

[35] J.H. Kim, H.J. Jo, S.M. Han, Y.J. Kim, S.Y. Kim, Recent advances in electrocatalysts for anion exchange membrane water electrolysis: design strategies and characterization approaches, Energy Mater. 5 (2025). https://doi.org/10.20517/energymater.2024.290.

[36] M. Mozakka, M. Salimi, M. Hosseinpour, Determining the challenges of transition to a hydrogen economy through developing a quantitative index, International Journal of Hydrogen Energy 56 (2024) 1301–1308. https://doi.org/10.1016/j.ijhydene.2023.12.297.

[37] M. Nasser, T.F. Megahed, S. Ookawara, H. Hassan, A review of water electrolysis-based systems for hydrogen production using hybrid/solar/wind energy systems, Environ. Sci. Pollut. Res. Int. 29 (2022) 86994–87018. https://doi.org/10.1007/s11356-022-23323-y.

[38] M. Hammad, S. Angel, A.K. Al-Kamal, A. Asghar, A. Said Amin, M.-A. Kräenbring, H.T. Wiedemann, V. Vinayakumar, M. Yusuf Ali, P. Fortugno, C. Kim, T.C. Schmidt, C.W. Kay, C. Schulz, D. Segets, H. Wiggers, Synthesis of novel LaCoO3/graphene catalysts as highly

efficient peroxymonosulfate activator for the degradation of organic pollutants, Chemical Engineering Journal 454 (2023) 139900. https://doi.org/10.1016/j.cej.2022.139900.

[39] M. Pidburtnyi, B. Zanca, C. Coppex, S. Jimenez-Villegas, V. Thangadurai, A Review on Perovskite-Type LaFeO 3 Based Electrodes for CO 2 Reduction in Solid Oxide Electrolysis Cells: Current Understanding of Structure–Functional Property Relationships, Chem. Mater. 33 (2021) 4249–4268. https://doi.org/10.1021/acs.chemmater.1c00771.

[40] Z. Shen, Y. Zhuang, W. Li, X. Huang, F.E. Oropeza, E.J.M. Hensen, J.P. Hofmann, M. Cui, A. Tadich, D. Qi, J. Cheng, J. Li, K.H.L. Zhang, Increased activity in the oxygen evolution reaction by Fe 4+ -induced hole states in perovskite La 1−x Sr x FeO 3, J. Mater. Chem. A 8 (2020) 4407–4415. https://doi.org/10.1039/C9TA13313E.

[41] Y. Zhu, W. Zhou, J. Yu, Y. Chen, M. Liu, Z. Shao, Enhancing Electrocatalytic Activity of Perovskite Oxides by Tuning Cation Deficiency for Oxygen Reduction and Evolution Reactions, Chem. Mater. 28 (2016) 1691–1697. https://doi.org/10.1021/acs.chemmater.5b04457.

[42] Y.D. Susanti, N. Afifah, R. Saleh, Ag modified LaMnO 3 nanoparticles for methylene blue degradation via photosonocatalytic activities, IOP Conf. Ser.: Mater. Sci. Eng. 496 (2019) 12037. https://doi.org/10.1088/1757-899X/496/1/012037.

[43] S. Thirumalairajan, K. Girija, N.Y. Hebalkar, D. Mangalaraj, C. Viswanathan, N. Ponpandian, Shape evolution of perovskite LaFeO3 nanostructures: a systematic investigation of growth mechanism, properties and morphology dependent photocatalytic activities, RSC Adv. 3 (2013) 7549. https://doi.org/10.1039/c3ra00006k.

[44] S. Zhou, X. Miao, X. Zhao, C. Ma, Y. Qiu, Z. Hu, J. Zhao, L. Shi, J. Zeng, Engineering electrocatalytic activity in nanosized perovskite cobaltite through surface spin-state transition, Nat. Commun. 7 (2016) 11510. https://doi.org/10.1038/ncomms11510.

[45] M.N. Iliev, M.V. Abrashev, H.-G. Lee, V.N. Popov, Y.Y. Sun, C. Thomsen, R.L. Meng, C.W. Chu, Raman spectroscopy of orthorhombic perovskitelike YMnO3 and LaMnO3, Phys. Rev. B 57 (1998) 2872–2877. https://doi.org/10.1103/PhysRevB.57.2872.

[46] M.V. Abrashev, A.P. Litvinchuk, M.N. Iliev, R.L. Meng, V.N. Popov, V.G. Ivanov, R.A. Chakalov, C. Thomsen, Comparative study of optical phonons in the rhombohedrally distorted perovskites LaAlO3 and LaMnO3, Phys. Rev. B 59 (1999) 4146–4153. https://doi.org/10.1103/PhysRevB.59.4146.

[47] A.F. Manchón-Gordón, P.E. Sánchez-Jiménez, J.S. Blázquez, A. Perejón, L.A. Pérez-Maqueda, Structural, Vibrational, and Magnetic Characterization of Orthoferrite LaFeO3 Ceramic Prepared by Reaction Flash Sintering, Materials (Basel) 16 (2023). https://doi.org/10.3390/ma16031019.

[48] Y. Huang, J. Liu, D. Cao, Z. Liu, K. Ren, K. Liu, A. Tang, Z. Wang, L. Li, S. Qu, Z. Wang, Separation of hot electrons and holes in Au/LaFeO3 to boost the photocatalytic activities both for water reduction and oxidation, International Journal of Hydrogen Energy 44 (2019) 13242–13252. https://doi.org/10.1016/j.ijhydene.2019.03.182.

[49] M. Połomska, B. Hilczer, J. Wolak, A. Pietraszko, M. Balcerzak, M. Jurczyk, J. Jakubowicz, XRD and Raman spectroscopy studies of (Bi 1– x La x FeO 3) 0.5 (PbTiO 3) 0.5 solid solution, Phase Transitions 87 (2014) 909–921. https://doi.org/10.1080/01411594.2014.953519.

[50] L. Tepech-Carrillo, A. Escobedo-Morales, A. Pérez-Centeno, E. Chigo-Anota, J.F. Sánchez-Ramírez, E. López-Apreza, J. Gutiérrez-Gutiérrez, Preparation of Nanosized LaCoO 3 through Calcination of a Hydrothermally Synthesized Precursor, Journal of Nanomaterials 2016 (2016) 1–7. https://doi.org/10.1155/2016/6917950.

[51] Y.-P. Zhang, H.-F. Liu, H.-L. Hu, R.-S. Xie, G.-H. Ma, J.-C. Huo, H.-B. Wang, Orientation-dependent structural and photocatalytic properties of LaCoO3 epitaxial nano-thin films, R. Soc. Open Sci. 5 (2018) 171376. https://doi.org/10.1098/rsos.171376.

[52] H.A. Martinez-Rodriguez, K. Onyekachi, A. Concha-Balderrama, G. Herrera-Pérez, J.A. Matutes-Aquino, J.F. Jurado, M.H. Bocanegra-Bernal, V.-H. Ramos-Sánchez, J.A. Duarte-Moller, A. Reyes-Rojas, Electronic configuration and magnetic properties of La0.7Ca0.3Mn1-xFexO3 perovskite NPs: The effect of a lower Fe3+ concentration, Journal of Alloys and Compounds 816 (2020) 152668. https://doi.org/10.1016/j.jallcom.2019.152668.

[53] D. Çoban Özkan, A. Türk, E. Çelik, Synthesis and characterizations of sol–gel derived LaFeO3 perovskite powders, J Mater Sci: Mater Electron 31 (2020) 22789–22809. https://doi.org/10.1007/s10854-020-04803-8.

[54] Y. Rao, Y. Zhang, J. Fan, G. Wei, D. Wang, F. Han, Y. Huang, J.-P. Croué, Enhanced peroxymonosulfate activation by Cu-doped LaFeO3 with rich oxygen vacancies: Compound-specific mechanisms, Chemical Engineering Journal 435 (2022) 134882. https://doi.org/10.1016/j.cej.2022.134882.

[55] J.X. Flores-Lasluisa, F. Huerta, D. Cazorla-Amorós, E. Morallón, Manganese oxides/LaMnO3 perovskite materials and their application in the oxygen reduction reaction, Energy 247 (2022) 123456. https://doi.org/10.1016/j.energy.2022.123456.

[56] B. Li, Q. Yang, Y. Peng, J. Chen, L. Deng, D. Wang, X. Hong, J. Li, Enhanced low-temperature activity of LaMnO3 for toluene oxidation: The effect of treatment with an acidic KMnO4, Chemical Engineering Journal 366 (2019) 92–99. https://doi.org/10.1016/j.cej.2019.01.139.

[57] G. Fang, K. Liu, M. Fan, J. Xian, Z. Wu, L. Wei, H. Tian, H. Jiang, W. Xu, H. Jin, J. Wan, Unveiling the electron configuration-dependent oxygen evolution activity of 2D porous Sr-substituted LaFeO 3 perovskite through microwave shock, Carbon Neutralization 2 (2023) 709–720. https://doi.org/10.1002/cnl2.94.

[58] M. Wang, B. Han, J. Deng, Y. Jiang, M. Zhou, M. Lucero, Y. Wang, Y. Chen, Z. Yang, A.T. N'Diaye, Q. Wang, Z.J. Xu, Z. Feng, Influence of Fe Substitution into LaCoO3

Electrocatalysts on Oxygen-Reduction Activity, ACS Appl. Mater. Interfaces 11 (2019) 5682–5686. https://doi.org/10.1021/acsami.8b20780.

[59] J. Qian, T. Wang, Z. Zhang, Y. Liu, J. Li, D. Gao, Engineered spin state in Ce doped LaCoO3 with enhanced electrocatalytic activity for rechargeable Zn-Air batteries, Nano Energy 74 (2020) 104948. https://doi.org/10.1016/j.nanoen.2020.104948.

[60] Y. Luo, J. Zuo, X. Feng, Q. Qian, Y. Zheng, D. Lin, B. Huang, Q. Chen, Good interaction between well dispersed Pt and LaCoO3 nanorods achieved rapid Co3+/Co2+ redox cycle for total propane oxidation, Chemical Engineering Journal 357 (2019) 395–403. https://doi.org/10.1016/j.cej.2018.09.158.

[61] M. Hammad, S. Angel, A.K. Al-Kamal, A. Asghar, M.-A. Kräenbring, A. Amin, H.T. Wiedemann, A.S. Amin, V. Vinayakumar, T.C. Schmidt, C.W. Kay, D. Segets, H. Wiggers, Spray-flame synthesis of LaCo0.2Mn0.8O3 for selective peroxymonosulfate activation into singlet oxygen towards efficient degradation of carbamazepine, Process Safety and Environmental Protection 194 (2025) 1347–1359. https://doi.org/10.1016/j.psep.2024.12.060.

[62] Z. Cao, J. Li, Y. Zhao, Q. Mei, Q. Wang, H. Cheng, Meta-kaolinite/LaFeCoO3 microsphere catalyst for photocatalytic persulfate activation: Enhanced removal of tetracycline hydrochloride, Chemical Engineering Journal 466 (2023) 143076. https://doi.org/10.1016/j.cej.2023.143076.

[63] R. Wang, C. Ye, H. Wang, F. Jiang, Z-Scheme LaCoO3/g-C3N4 for Efficient Full-Spectrum Light-Simulated Solar Photocatalytic Hydrogen Generation, ACS Omega 5 (2020) 30373–30382. https://doi.org/10.1021/acsomega.0c03318.

[64] M. Khalifa, A.M. El Sayed, S.M. Kassem, E. Tarek, Synthesis, structural, optical, and thermal properties of LaFeO3/Poly(methyl methacrylate)/Poly(vinyl acetate) nanocomposites for radiation shielding, Sci. Rep. 14 (2024) 3672. https://doi.org/10.1038/s41598-024-54207-5.

[65] P. Lang, N.E. Schneider, F.J. Huber, S. Will, Characterization of the SpraySyn 2.0 burner: Droplet diameters, flame stability and particle sizes, Applications in Energy and Combustion Science 22 (2025) 100324. https://doi.org/10.1016/j.jaecs.2025.100324.

[66] S. Abbot, Solubility Science: Principles and Practice, Creative Commons BY-ND, 2017.

[67] O. Anwar, S. Bapat, J. Ahmed, X. Xie, J. Sun, D. Segets, Hansen parameter evaluation for the characterization of titania photocatalysts using particle size distributions and combinatorics, Nanoscale 14 (2022) 13593–13607. https://doi.org/10.1039/d2nr02711a.

[68] A.S. Amin, D. Lerche, A.S. Odungat, S.U. Boehm, T. Koch, F. Özcan, D. Segets, 2024. A Procedure for Rational Probe Liquids Selection to Determine Hansen Solubility Parameters. ChemCatChem, e202301393. https://doi.org/10.1002/cctc.202301393.

[69] S. Bapat, D. Segets, Sedimentation Dynamics of Colloidal Formulations through Direct Visualization: Implications for Fuel Cell Catalyst Inks, ACS Appl. Nano Mater. 3 (2020) 7384–7391. https://doi.org/10.1021/acsanm.0c01467.

[70] S. Süß, T. Sobisch, W. Peukert, D. Lerche, D. Segets, Determination of Hansen parameters for particles: A standardized routine based on analytical centrifugation, Advanced Powder Technology 29 (2018) 1550–1561. https://doi.org/10.1016/j.apt.2018.03.018.

[71] O. Anwar, A.S. Amin, A. Amin, M.-A. Kräenbring, F. Özcan, D. Segets, 2023. Determination of Hansen Parameters of Nanoparticles: A Comparison of Two Methods Using Titania, Carbon Black, and Silicon/Carbon Composite Materials. Part & Part Syst Charact 40, 2300050. https://doi.org/10.1002/ppsc.202300050.

[72] S. Khandavalli, J.H. Park, N.N. Kariuki, D.J. Myers, J.J. Stickel, K. Hurst, K.C. Neyerlin, M. Ulsh, S.A. Mauger, Rheological Investigation on the Microstructure of Fuel Cell Catalyst Inks, ACS Appl. Mater. Interfaces 10 (2018) 43610–43622. https://doi.org/10.1021/acsami.8b15039.

[73] L. de Sousa, C. Harmoko, N. Benes, G. Mul, Optimizing the Ink Formulation for Preparation of Cu-Based Gas Diffusion Electrodes Yielding Ethylene in Electroreduction of CO 2, ACS EST Eng. 1 (2021) 1649–1658. https://doi.org/10.1021/acsestengg.1c00228.

[74] Z. Xu, J. Liang, L. Zhou, Photo-Fenton-like degradation of azo dye methyl orange using synthetic ammonium and hydronium jarosite, Journal of Alloys and Compounds 546 (2013) 112–118. https://doi.org/10.1016/j.jallcom.2012.08.087.

[75] G. Mladin, M. Ciopec, A. Negrea, N. Duteanu, P. Negrea, P. Ianasi, C. Ianași, Silica- Iron Oxide Nanocomposite Enhanced with Porogen Agent Used for Arsenic Removal, Materials (Basel) 15 (2022). https://doi.org/10.3390/ma15155366.

[76] G.M. Estrada-Villegas, G. Morselli, M.J.A. Oliveira, G. González-Pérez, A.B. Lugão, PVGA/Alginate-AgNPs hydrogel as absorbent biomaterial and its soil biodegradation behavior, Polym. Bull. 77 (2020) 4147–4166. https://doi.org/10.1007/s00289-019-02966-x.

[77] A. Taheri Najafabadi, A.A. Khodadadi, M.J. Parnian, Y. Mortazavi, Atomic layer deposited Co/γ-Al2O3 catalyst with enhanced cobalt dispersion and Fischer–Tropsch synthesis activity and selectivity, Applied Catalysis A: General 511 (2016) 31–46. https://doi.org/10.1016/j.apcata.2015.11.027.

[78] T.-D. Hoang, N. Nghiem, Recent Developments and Current Status of Commercial Production of Fuel Ethanol, Fermentation 7 (2021) 314. https://doi.org/10.3390/fermentation7040314.

[79] E. Newes, C. Clark, L. Vimmerstedt, S. Peterson, D. Burkholder, D. Korotney, D. Inman, Expanding Ethanol Production in the United States: The Roles of Policy, Price, and Demand, Energy Policy 161 (2021) 1–10. https://doi.org/10.1016/j.enpol.2021.112713.

[80] J. Areola Hernandez, G.S. Uddin, A. Dutta, A. Ahmed, S.H. Kang, Are ethanol markets globalized or regionalized?, Physica A: Statistical Mechanics and its Applications 551 (2020) 124094. https://doi.org/10.1016/j.physa.2019.124094.

[81] A. Bastianin, M. Galeotti, M. Manera, Causality and predictability in distribution: The ethanol–food price relation revisited, Energy Economics 42 (2014) 152–160. https://doi.org/10.1016/j.eneco.2013.12.014.

[82] P.H. Hoeckel, A.M. Alvim, J.P. Pontes, J. Dias, The Ethanol Market and Its Relation to the Price of Agricultural Commodities, Energies 16 (2023) 2788. https://doi.org/10.3390/en16062788.

[83] A.S. Nascimento Filho, H. Saba, R.G.O. dos Santos, J.G.A. Calmon, M.L.V. Araújo, E.M.F. Jorge, T.B. Murari, Analysis of Hydrous Ethanol Price Competitiveness after the Implementation of the Fossil Fuel Import Price Parity Policy in Brazil, Sustainability 13 (2021) 9899. https://doi.org/10.3390/su13179899.

[84] T. Mizik, L. Nagy, Z. Gabnai, A. Bai, The Major Driving Forces of the EU and US Ethanol Markets with Special Attention Paid to the COVID-19 Pandemic, Energies 13 (2020) 5614. https://doi.org/10.3390/en13215614.

[85] K. Guan, J. Shen, G. Liu, J. Zhao, H. Zhou, W. Jin, Spray-evaporation assembled graphene oxide membranes for selective hydrogen transport, Separation and Purification Technology 174 (2017) 126–135. https://doi.org/10.1016/j.seppur.2016.10.012.

[86] Y. Luo, J. Zhang, Z. Zhou, J.P. Aguilar-Lopez, R. Greco, T. Bogaard, Effects of dynamic changes of desiccation cracks on preferential flow: experimental investigation and numerical modeling, Hydrol. Earth Syst. Sci. 27 (2023) 783–808. https://doi.org/10.5194/hess-27-783-2023.

[87] A.S. Odungat, L. Grebener, O. Pasdag, T.B. Nguyen, Y. Zhu, S. Kohsakowski, I. Radev, F. Özcan, D. Segets, 2025. A Multiscale Pore Analysis Method for Polymer Electrolyte Membrane Fuel Cell Catalyst Layers Validated and Exemplified by Correlating Microstructure with Production Process Parameters. Adv Energy and Sustain Res, 2500043. https://doi.org/10.1002/aesr.202500043.

[88] J. Islam, B.S. Yoon, P.T. Thien, C.H. Ko, S.-K. Kim, Enhancing oxygen evolution reaction performance in PEM water electrolyzers through support pore structure optimization, Catalysis Today 425 (2024) 114349. https://doi.org/10.1016/j.cattod.2023.114349.

[89] Y. Li, Z. Kan, L. Jia, D. Zhang, Y. Hong, J. Liu, H. Huang, S. Li, S. Liu, Elucidating the Role of Mass Transfer in Electrochemical Redox Reactions on Electrospun Fibers, Trans. Tianjin Univ. 29 (2023) 313–320. https://doi.org/10.1007/s12209-023-00369-8.

[90] K. Tsuburaya, K. Obata, K. Nagato, K. Takanabe, Porous Substrate Optimization for Efficient Water Electrolysis: Uncovering Electrocatalysts, Electrolyte, and Bubble Dynamics Effects, ACS Sustainable Chem. Eng. 12 (2024) 16308–16319. https://doi.org/10.1021/acssuschemeng.4c05790.

[91] A. Vazhayil, J. Thomas, N. Thomas, Cobalt doping in LaMnO3 perovskite catalysts – B site optimization by solution combustion for oxygen evolution reaction, Journal of Electroanalytical Chemistry 918 (2022) 116426. https://doi.org/10.1016/j.jelechem.2022.116426.

[92] X. Liu, H. Gong, T. Wang, H. Guo, L. Song, W. Xia, B. Gao, Z. Jiang, L. Feng, J. He, Cobalt-Doped Perovskite-Type Oxide LaMnO3 as Bifunctional Oxygen Catalysts for Hybrid Lithium-Oxygen Batteries, Chem. Asian J. 13 (2018) 528–535. https://doi.org/10.1002/asia.201701561.

[93] W.G. Hardin, J.T. Mefford, D.A. Slanac, B.B. Patel, X. Wang, S. Dai, X. Zhao, R.S. Ruoff, K.P. Johnston, K.J. Stevenson, Tuning the Electrocatalytic Activity of Perovskites through Active Site Variation and Support Interactions, Chem. Mater. 26 (2014) 3368–3376. https://doi.org/10.1021/cm403785q.

[94] H. He, J. Chen, D. Zhang, F. Li, X. Chen, Y. Chen, L. Bian, Q. Wang, P. Duan, Z. Wen, X. Lv, Modulating the Electrocatalytic Performance of Palladium with the Electronic Metal–Support Interaction: A Case Study on Oxygen Evolution Reaction, ACS Catal. 8 (2018) 6617–6626. https://doi.org/10.1021/acscatal.8b00460.

[95] A. Olean-Oliveira, A.R. Khan, B. Toplak, I. Spanos, M. Hammad, A. Jain, U. Hagemann, H. Wiggers, D. Segets, V. Čolić, Intrinsic Activity and Mechanistic Insights in $LaCoO_3$ OER Catalysts Induced by Support Material, Electrochimica Acta (2025) 147874. https://doi.org/10.1016/j.electacta.2025.147874.

[96] Yun Bao, Kensaku Nagasawa, Yoshiyuki Kuroda, Shigenori Mitsushima, Current Measurement and Electrochemical Characterization of Gas Evolution Reactions on a Rotating Ring-Disk Electrode, Electrocatalysis 11 (2020) 301–308. https://doi.org/10.1007/s12678-020-00589-9.

[97] A.R.C. Bredar, A.L. Chown, A.R. Burton, B.H. Farnum, Electrochemical Impedance Spectroscopy of Metal Oxide Electrodes for Energy Applications, ACS Appl. Energy Mater. 3 (2020) 66–98. https://doi.org/10.1021/acsaem.9b01965.

[98] X. Mao, A.C. Foucher, E.A. Stach, R.J. Gorte, Changes in Ni-NiO equilibrium due to LaFeO3 and the effect on dry reforming of CH4, Journal of Catalysis 381 (2020) 561–569. https://doi.org/10.1016/j.jcat.2019.11.040.

[99] R. Thalinger, M. Gocyla, M. Heggen, R. Dunin-Borkowski, M. Grünbacher, M. Stöger-Pollach, D. Schmidmair, B. Klötzer, S. Penner, Ni–perovskite interaction and its structural and catalytic consequences in methane steam reforming and methanation reactions, Journal of Catalysis 337 (2016) 26–35. https://doi.org/10.1016/j.jcat.2016.01.020.

[100] Y.K. Kim, W.T. Jun, D.H. Youn, J.S. Lee, Metal substrates activate NiFe(oxy)hydroxide catalysts for efficient oxygen evolution reaction in alkaline media, Journal of Alloys and Compounds 901 (2022) 163689. https://doi.org/10.1016/j.jallcom.2022.163689.

[101] F. Qi, J. Peng, Z. Liang, J. Guo, J. Liu, T. Fang, H. Mao, Strong metal-support interaction (SMSI) in environmental catalysis: Mechanisms, application, regulation strategies, and breakthroughs, Environ. Sci. Ecotechnol. 22 (2024) 100443. https://doi.org/10.1016/j.ese.2024.100443.

[102] Y. Li, M. Liu, Y. Liu, Y. Shen, Y. Pan, H. Jin, Reaction kinetics of Ni-Fe oxygen carriers with high performance for chemical looping hydrogen production, Chemical Engineering Journal 499 (2024) 156067. https://doi.org/10.1016/j.cej.2024.156067.

[103] V. Tripkovic, H.A. Hansen, J.M. Garcia-Lastra, T. Vegge, Comparative DFT+U and HSE Study of the Oxygen Evolution Electrocatalysis on Perovskite Oxides, J. Phys. Chem. C 122 (2018) 1135–1147. https://doi.org/10.1021/acs.jpcc.7b07660.

[104] R. Martínez-Hincapié, J. Wegner, M.U. Anwar, A. Raza-Khan, S. Franzka, S. Kleszczynski, V. Čolić, The determination of the electrochemically active surface area and its effects on the electrocatalytic properties of structured nickel electrodes produced by additive manufacturing, Electrochimica Acta 476 (2024) 143663. https://doi.org/10.1016/j.electacta.2023.143663.

[105] S. Anantharaj, P.E. Karthik, S. Noda, The Significance of Properly Reporting Turnover Frequency in Electrocatalysis Research, Angew. Chem. Int. Ed Engl. 60 (2021) 23051–23067. https://doi.org/10.1002/anie.202110352.

[106] E. Budiyanto, S. Salamon, Y. Wang, H. Wende, H. Tüysüz, Phase Segregation in Cobalt Iron Oxide Nanowires toward Enhanced Oxygen Evolution Reaction Activity, JACS Au 2 (2022) 697–710. https://doi.org/10.1021/jacsau.1c00561.

[107] J.A. Haber, Y. Cai, S. Jung, C. Xiang, S. Mitrovic, J. Jin, A.T. Bell, J.M. Gregoire, Discovering Ce-rich oxygen evolution catalysts, from high throughput screening to water electrolysis, Energy Environ. Sci. 7 (2014) 682–688. https://doi.org/10.1039/C3EE43683G.

[108] J.P. Kollender, A.I. Mardare, A.W. Hassel, Multi-Scanning Droplet Cell Microscopy (multi-SDCM) for truly parallel high throughput electrochemical experimentation, Electrochimica Acta 179 (2015) 32–37. https://doi.org/10.1016/j.electacta.2015.04.103.

[109] A. Angulo, P. van der Linde, H. Gardeniers, M. Modestino, D. Fernández Rivas, Influence of Bubbles on the Energy Conversion Efficiency of Electrochemical Reactors, Joule 4 (2020) 555–579. https://doi.org/10.1016/j.joule.2020.01.005.

[110] T. Lazaridis, B.M. Stühmeier, H.A. Gasteiger, H.A. El-Sayed, Capabilities and limitations of rotating disk electrodes versus membrane electrode assemblies in the investigation of electrocatalysts, Nat Catal 5 (2022) 363–373. https://doi.org/10.1038/s41929-022-00776-5.

[111] J. Knöppel, M. Möckl, D. Escalera-López, K. Stojanovski, M. Bierling, T. Böhm, S. Thiele, M. Rzepka, S. Cherevko, On the limitations in assessing stability of oxygen evolution catalysts using aqueous model electrochemical cells, Nat. Commun. 12 (2021) 2231. https://doi.org/10.1038/s41467-021-22296-9.

[112] L. An, R. Chen, Y. Li (Eds.), Flow Cells for Electrochemical Energy Systems: Fundamentals and Applications, 1st ed., Springer International Publishing; Imprint Springer, Cham, 2023.

[113] C. Li, J.-B. Baek, The promise of hydrogen production from alkaline anion exchange membrane electrolyzers, Nano Energy 87 (2021) 106162. https://doi.org/10.1016/j.nanoen.2021.106162.

[114] R. Baddour-Hadjean, J.-P. Pereira-Ramos, Raman microspectrometry applied to the study of electrode materials for lithium batteries, Chem. Rev. 110 (2010) 1278–1319. https://doi.org/10.1021/cr800344k.

[115] H.R. Barai, A.N. Banerjee, S.W. Joo, Improved electrochemical properties of highly porous amorphous manganese oxide nanoparticles with crystalline edges for superior supercapacitors, Journal of Industrial and Engineering Chemistry 56 (2017) 212–224. https://doi.org/10.1016/j.jiec.2017.07.014.

[116] J. Wang, X. Ma, F. Qu, A.M. Asiri, X. Sun, Fe-Doped Ni2P Nanosheet Array for High-Efficiency Electrochemical Water Oxidation, Inorg. Chem. 56 (2017) 1041–1044. https://doi.org/10.1021/acs.inorgchem.6b02808.

[117] F. Bao, E. Kemppainen, I. Dorbandt, F. Xi, R. Bors, N. Maticiuc, R. Wenisch, R. Bagacki, C. Schary, U. Michalczik, P. Bogdanoff, I. Lauermann, R. van de Krol, R. Schlatmann, S. Calnan, Host, Suppressor, and Promoter—The Roles of Ni and Fe on Oxygen Evolution Reaction Activity and Stability of NiFe Alloy Thin Films in Alkaline Media, ACS Catal. 11 (2021) 10537–10552. https://doi.org/10.1021/acscatal.1c01190.

[118] C. Lv, H. Chen, M. Hu, T. Ai, H. Fu, Nano-oxides washcoat for enhanced catalytic oxidation activity toward the perovskite-based monolithic catalyst, Environ. Sci. Pollut. Res. Int. 28 (2021) 37142–37157. https://doi.org/10.1007/s11356-021-13354-2.

[119] N.S. Chaudhari, S.S. Warule, S. Muduli, B.B. Kale, S. Jouen, B. Lefez, B. Hannoyer, S.B. Ogale, Maghemite (hematite) core (shell) nanorods via thermolysis of a molecular solid of Fe-complex, Dalton Trans. 40 (2011) 8003–8011. https://doi.org/10.1039/c1dt10319a.

[120] S.P. Schwaminger, P. Fraga-García, F. Selbach, F.G. Hein, E.C. Fuß, R. Surya, H.-C. Roth, S.A. Blank-Shim, F.E. Wagner, S. Heissler, S. Berensmeier, Bio-nano interactions: cellulase on iron oxide nanoparticle surfaces, Adsorption 23 (2017) 281–292. https://doi.org/10.1007/s10450-016-9849-y.

[121] R. Wei, G. Fu, H. Qi, H. Liu, Tuning the high-entropy perovskite as efficient and reliable electrocatalysts for oxygen evolution reaction, RSC Adv. 14 (2024) 18117–18125. https://doi.org/10.1039/d4ra02680b.

[122] W. Li, F. Yang, P. Xiong, Y. Jia, J. Liu, X. Yan, X. Chen, Effect of Bi-doping on the electrocatalytic properties of LaFeO3 powders prepared by sol–gel method, J Mater Sci 54 (2019) 7460–7468. https://doi.org/10.1007/s10853-019-03443-6.

[123] C. Huang, J. Wu, Y.-T. Chen, M. Tian, A.I. Rykov, B. Hou, J. Lin, C.-R. Chang, X. Pan, J. Wang, A. Wang, X. Wang, In situ encapsulation of iron(0) for solar thermochemical syngas production over iron-based perovskite material, Commun Chem 1 (2018). https://doi.org/10.1038/s42004-018-0050-y.

[124] F. Bai, J. Schulwitz, T. Priamushko, U. Hagemann, A. Kostka, M. Heidelmann, S. Cherevko, M. Muhler, T. Li, Correlating atomic-scale structural and compositional details of Ca-doped LaCoO3 perovskite nanoparticles with activity and stability towards the oxygen evolution reaction, Journal of Catalysis 438 (2024) 115697. https://doi.org/10.1016/j.jcat.2024.115697.

[125] W. Hu, Q. Liu, T. Lv, F. Zhou, Y. Zhong, Impact of interfacial CoOOH on OER catalytic activities and electrochemical behaviors of bimetallic CoxNi-LDH nanosheet catalysts, Electrochimica Acta 381 (2021) 138276. https://doi.org/10.1016/j.electacta.2021.138276.

[126] J. Huang, H. Sheng, R.D. Ross, J. Han, X. Wang, B. Song, S. Jin, Modifying redox properties and local bonding of Co3O4 by CeO2 enhances oxygen evolution catalysis in acid, Nat. Commun. 12 (2021) 3036. https://doi.org/10.1038/s41467-021-23390-8.

[127] H. Petlund, A. Pokle, A. Chatzitakis, Suppression of surface amorphization during oxygen evolution reaction in A-site deficient perovskite oxides, J. Phys. Energy 7 (2025) 25010. https://doi.org/10.1088/2515-7655/adb2c0.

[128] A. Bergmann, E. Martinez-Moreno, D. Teschner, P. Chernev, M. Gliech, J.F. de Araújo, T. Reier, H. Dau, P. Strasser, Reversible amorphization and the catalytically active state of crystalline Co3O4 during oxygen evolution, Nat. Commun. 6 (2015) 8625. https://doi.org/10.1038/ncomms9625.

[129] Z. Li, Y. Xie, Z. Huang, Y. Su, C. Sun, J. Fu, H. Wei, F. Wu, G. Ou, Amorphization of LaCoO 3 Perovskite Nanostructures for Efficient Oxygen Evolution, ACS Appl. Nano Mater. 5 (2022) 14209–14215. https://doi.org/10.1021/acsanm.2c02982.

[130] W. Cai, R. Chen, H. Yang, H.B. Tao, H.-Y. Wang, J. Gao, W. Liu, S. Liu, S.-F. Hung, B. Liu, Amorphous versus Crystalline in Water Oxidation Catalysis: A Case Study of NiFe Alloy, Nano Lett. 20 (2020) 4278–4285. https://doi.org/10.1021/acs.nanolett.0c00840.

[131] A. Indra, P.W. Menezes, N.R. Sahraie, A. Bergmann, C. Das, M. Tallarida, D. Schmeißer, P. Strasser, M. Driess, Unification of catalytic water oxidation and oxygen reduction reactions: amorphous beat crystalline cobalt iron oxides, J. Am. Chem. Soc. 136 (2014) 17530–17536. https://doi.org/10.1021/ja509348t.

[132] I. Vincent, E.-C. Lee, H.-M. Kim, Comprehensive impedance investigation of low-cost anion exchange membrane electrolysis for large-scale hydrogen production, Sci. Rep. 11 (2021) 293. https://doi.org/10.1038/s41598-020-80683-6.

6. Abbreviations

Table 3. Abbreviations used in the research paper.

Abbreviation	Full name	Abbreviation	Full name
AC	Analytical centrifuge	LSV	Linear sweep voltammetry
AEM	Adsorbate evolution mechanism	MOF	Metal-organic frameworks
AFM	Atomic force microscopy	OCP	Open circuit potential
BET	Brunauer-Emmett-Teller method	OER	Oxygen evolution reaction
C_{dl}	Double-layer capacitance	PL	Probe liquid
CE	Counter electrode	Pristine	Pristine material
CP	Chronopotentiometry	PTFE	Polytetrafluoroethylene
CV	Cyclic voltammetry	RDE	Rotating disc electrode
ECSA	Electrochemically active surface area	RE	Reference electrode
EDX	Energy-dispersive X-ray analysis	RHE	Reversible hydrogen electrode
EEC	Electrical equivalent circuits	RMS	Root mean square
EIS	Electrochemical impedance spectroscopy	SDC	Scanning droplet cell
FTIR	Fourier transform infrared spectroscopy	SEM	Scanning electron microscope
GCE	Glassy-carbon electrode	SFS	Spray-flame synthesis
GIXRD	Grazing incidence mode X-ray diffraction	slm	Standard liter per minute
HRTEM	High resolution transmission electron microscopy	SMSI	Strong metal-support interaction
HSP	Hansen solubility parameter	Spent-60	Material tested for 24 h at 60 °C
		Spent-RT	Material tested for 24 h at room temperature
ICP-OES	Inductively coupled plasma optical emission spectrometry	TEM	Transmission electron microscopy
La-based	Lanthanum-based	TOF	Turnover frequency
LCO	$LaCoO_3$	XPS	X-ray photoelectron spectroscopy

LFO	$LaFeO_3$	XRD	X-ray diffraction
LMO	$LaMnO_3$	3D	Three-dimensional
LOM	Lattice oxygen mechanism		